A multivariate regression parametric study on DEM input parameters of free-flowing and cohesive powders with experimental data-based validation

Bilal El-Kassem[1,2] · Nizar Salloum[2] · Thomas Brinz[2] · Yousef Heider[1] · Bernd Markert[1]

Abstract

One of the key challenges in the implementation of discrete element method (DEM) to model powder's flow is the appropriate selection of material parameters, where empirical approaches are mostly applied. The aim of this study is to develop an alternative systematic numerical approach that can efficiently and accurately predict the influence of different DEM parameters on various sought macroscopic responses, where, accordingly, model validation based on experimental data is applied. Therefore, design of experiment and multivariate regression analysis, using an optimized quadratic D-optimal design model and new analysis tools, i.e., adjusted response and Pareto graphs, are applied. A special focus is laid on the impact of six DEM microscopic input parameters (i.e., coefficients of static and rolling friction, coefficient of restitution, particle size, Young's modulus and cohesion energy density) on five macroscopic output responses (i.e., angle of repose, porosity, mass flow rate, translational kinetic energy and computation time) using angle of repose tests applied to free-flowing and cohesive powders. The underlying analyses and tests show, for instance, the substantial impact of the rolling friction coefficient and the minor role of the static friction coefficient or the particle size on the angle of repose in cohesive powders. In addition, in both powders, the porosity parameter is highly influenced by the static and rolling friction coefficients.

Keywords Discrete element method · Free-flowing powder · Cohesive powder · Design of experiment · Multivariate regression analysis · Angle of repose

1 Introduction

One of the big challenges in the pharmaceutical industry is to optimize the powder solid handling process performance. This significantly relies on the flowability of the granular material in different process stages including hopper discharge, powder feeding, blending, mixing and die filling. Flowability, which describes the behavior of powder, is dependent on a range of fundamental powder properties. The flow properties of powders can be affected by various essential particle properties, including mean particle size and distribution, particle shape, surface roughness and

moisture content. Powder flow also depends on the interparticle interactions where, for instance, flowability decreases with increasing cohesiveness of the powder. According to Parker et al. [1], cohesion is defined as the bonding or joining of two particles of the same material. A bulk solid with poor flowability is considered to be cohesive, which is due to the relatively high interparticle forces compared to the particle weight [2]. The inherent strength of the interparticle forces of attraction (often called cohesive forces) is derived from a combination of van der Waals forces and electrostatic charge on the surface of the particles. These forces hold particles close to their neighbors and thus result in the formation of agglomerates. Capillary force (liquid bridge), van der Waals force, electrostatic force and the weight force are all considered as adhesive forces, mainly interparticle forces between the particles and the wall. Understanding the physical meaning of these properties and their impact on the final product design is crucial in the development and successful production of solid dosage forms.

✉ Yousef Heider
heider@iam.rwth-aachen.de

1 Institute of General Mechanics, RWTH Aachen University, Templergraben 64, 52062 Aachen, Germany

2 Robert Bosch Packaging Technology GmbH, Stuttgarter Str. 130, 71332 Waiblingen, Germany

During their operation, industrial machines dealing with powders might encounter diverse problems which, due to their complexity, are most of the time difficult to analyze by traditional means. Therefore, many studies are extensively applied to optimize their operations, to deeply understand their functionalities, and to predict possible defects. For modeling a granular material, several numerical approaches on different scales and with different degrees of complexity and computational costs can be found in the literature. The microscopic discrete element method (DEM) (Cundall and Strack [3]) accounts for the most popular schemes and provides an effective approach for the understanding of granular material's mechanical behavior and flowability on the microscale. In particular, DEM is a particle-based method used to model movement and interaction of bulk material [2]. Each particle is treated individually and its motion is described by Newton's equation of motion. A soft-sphere approach is used, where colliding particles are allowed to slightly overlap resulting in a repulsive force [4]. DEM has been proven to be an important and efficient tool in several fields such as powder metallurgy, chemical engineering, pharmaceuticals and agriculture. To mention some, DEM simulations have been applied in granular-related processes such as die filling [5], bulk compression [6], powder mixing [7], particles packing [8, 9], agglomerates fragmentation [10], flow in screw conveyor [11–13] and outflow from a hopper. Apart from DEM, other approaches, such as continuum porous media mechanics, can be applied to compute granular material mechanical responses on larger (macroscopic) scales and capture important behaviors such as wave propagation or fracture [14–16]. However, these approaches assume the continuity of the matter and cannot explicitly capture the interactions between the particles. Therefore, the focus in this work would be merely on DEM approach.

One of the most challenging aspects in applying efficiently the DEM numerical approach is choosing the appropriate contact models and then finding the right values of the input particle parameters involved in any used model. As particles introduced in granular materials are considerably small in size, measuring the properties of every single particle is considered very costly, challenging and time-consuming. Yet, some trials using atomic force microscopy have been given to measuring the individual particles' yield stress [17], Young's modulus (Y) [18] and interfacial energy [19]. The state-of-the-art approaches for calibration of DEM parameters in most cases are based on the trial-and-error, where the track of the calibration process is lost in many cases by the human calibrators, especially when many factors are involved [20]. It is often the case that the DEM model is calibrated against bulk measurements and the input parameters are adjusted until the outputs of the model match with the experimental observations [21]. Therefore, it is of great interest for researchers to optimize

the process of calibration. In the literature, different tools for DEM parameters calibration, some of which are (semi-)automated, can be found. Al-Hashemi et al. [22] presented an extensive review related to the angle of repose (AoR), methods of measurements, appropriate applications and the influencing factors of different parameters. Coetzee [23] discussed different DEM calibration approaches covered in the literature over the last 25 years to assist future researchers to improve on the existing ones. Liu et al. [24] investigated the impact of particle aspect ratio on the DEM simulation output in studying powder flow from hoppers. The authors developed a modified description of the classic Beverloo equation. Zhou et al. [25] studied the influence of particle–particle and particle–wall coefficients of friction, i.e., static and sliding on the AoR of a sandpile test. They constructed a power-law relationship between measured AoR and the input parameters and showed that all friction coefficients followed a positive dependency, whereas particle size followed a significant negative dependency. Yan et al. [26] utilized a multilevel statistical analysis approach on hopper flow in DEM to study the influence of coefficients of friction and restitution, as well as Young's modulus. Using principal component analysis (PCA), the empirical power-law approach was found to agree with a semiempirical, which compared AoR to contact model parameter sensitivity matrices. The results in all cases showed that the coefficient of static friction was the critical parameter, which allows the gap to be bridged between bulk and interparticle interactions. In addition, it is shown that reducing the shear modulus (i.e., from 10^7 and 10^{11} Pa) proved to have an insignificant effect on the powder flowability using free-flowing material which was also proven by Lommen et al. [27].

Boukouvala et al. [28] used a reduced-order approach to assess the importance of DEM parameters where PCA was coupled with surrogate models mapping which identified key areas of sensitivity. Major principal components enabled a reduced and computationally more efficient model to be engaged for future simulations. El Kassem et al. [29] calibrated the AoR of a pharmaceutical powder by varying coefficients of rolling friction and restitution using DoE, while determining the coefficient of static friction using the FT4 powder rheometer. Souihi et al. [30] used a statistical design of experiments (DoE) to provide a more efficient approach in investigating roller compaction. Orthogonal partial least squares (PLS) regression was used to analyze the results of a reduced central composite face-centered design in DoE. Wilkinson et al. [31] added that such approach using regression analysis has not been used so far for DEM simulations, but is highly recommended for developing more universal models for particle flow in a more efficient way. He proved that the Y has a negative impact on flow energy under specific conditions using a cohesive material. In this work, the effect of Y with the combination of varying the particle size

in the same design model is studied which was not covered by [26] and [31]. To add up, Johnstone [32] used DoE to perform different calibration and validation methods based on experimental measurements. Benvenuti et al. [33] used artificial neural network to identify DEM simulation parameters. However, Rackl et al. [34] used a methodical calibration approach based on Latin hypercube sampling and Kriging, where they showed that different parameter combinations might lead to similar results. Wei et al. [35] studied the effect of three particle shapes on the AoR and bottom porosity distribution of a heap formed by natural piling using DEM. They found that the static friction has the major impact on the AoR and the porosity followed with the particle shape. Moreover, Li et al. [36] investigated the influence of three factors, namely moisture content, rice velocity and depth of the rice layer on the porosity of the flowing rice layer based on mass conservation and the poroelasticity theory. These results showed that the latter three factors have a significant influence on the porosity. Cheng et al. [37] developed a DEM calibration approach of granular soils based on the sequential quasi-Monte Carlo (SQMC) filter. They calibrated the micromechanical parameters of the contact laws against the stress–strain behavior of Toyoura sand in drained triaxial compression conditions at different confining pressures. Do et al. [38] developed two automated DEM calibration approaches using genetic and direct optimization algorithms.

Moreover, in addition to the calibration process, one of the existing challenges in DEM is the high computational cost needed to perform real industrial-scale simulations because of the extremely large number of particles being studied simultaneously at every time step. One of the most efficient approaches utilized to overcome this "obstacle" is to scale up the particle sizes and thus, reduce the total number of particles in the system according to coarse-graining method [39–43]. The most challenging issue in following such a method lies in adapting the material properties in such a way that compensates for the enlargement of the particles. In this study, the coarse-graining scheme proposed by Bierwisch et al. [42] was applied. The basis of this scheme is the preservation of the kinetic and gravitational potential energy densities as well as the volume fraction of particles as the original system with unscaled particles.

In this study, a novel simplified semiautomated parametric study and calibration approach is developed using an optimized multivariate regression analysis (MVRA). Initially, experimental powder characterization and AoR tests are performed. DoE method, using quadratic D-optimal design model, are applied for the sake of minimizing the number of simulations in an optimized way that retains high significance by recommending suitable possible combinations between DEM microscopic input parameters that should be tested together. The D-optimal design proved its efficiency by building a robust model by saving a lot of time

and efforts compared to other models that require much more data points such as full factorial design. The proposed simulation runs from the DoE were performed in a parallel manner by implementing a code programming through the open-source software LIGGGHTS® [44]. The studied microscopic input parameters are the coefficients of static and rolling friction, coefficient of restitution, particle size, Young's modulus and cohesion energy density. The effects of these input parameters on five macroscopic output responses (targets), i.e., AoR, porosity, mass flow rate, translational kinetic energy and computation time, are studied through MVRA, using Cornerstone software, to find out which parameters and in what sense do they influence these targets. This systematic approach was done for a free-flowing powder and a cohesive powder, namely SpheroLac 100 and Inhalac 251, respectively. This method gives a more robust understanding of the impact of the interparticle input parameters on the flowability of the powders at different ranges (low, center and high) by tuning them in a methodical way rather than trial-and-error. Since it is possible to have the same AoR with various DEM input parameter combinations [45, 46], the porosity is measured along with the AoR in DEM simulations in order to determine a more reliable and practical value for the studied input parameters. Accordingly, a prediction model is built to validate the regression analysis and to calibrate our experimental AoR and porosity values by selecting one optimized parameter combination.

2 Materials and methods

2.1 Materials

In this study, two pharmaceutical crystalline lactose monohydrate powders, purchased from MEGGLE Wasserburg GmbH & Co. KG (Germany), were selected. SpheroLac 100 was used to model the free-flowing powder, and InhaLac 251 was utilized to model the cohesive one. They are mainly characterized by different particle sizes, which in turn affect their flowability. SpheroLac 100 is mainly used in capsule filling, blends, premixes, sachets, triturations, whereas InhaLac 251 is a dry powder inhaler used in capsule- or blister-based formulations.

2.2 Experimental angle of repose (AoR)

The AoR is defined as the slope of a poured conical pile of loose uncompacted bulk solid material [18]. It is a characteristic related to the cohesiveness of the powder [47] and used as a common method to characterize powders according to their flowability [48–51]. It is a common method to calibrate DEM simulation parameters, where the angle at which a heap of powder settles depends on the strength

of the interparticulate friction. This simple test case was chosen in order to perform a parametric study of the DEM microscopic input parameters. As depicted in Fig. 1, a funnel made of 1.4404 stainless steel was placed above a catching container made of borosilicate 3.3 glass. Initially, the funnel was loosely filled with 5 g of powder where the lower opening of the funnel was closed. Then, the funnel was opened to let the powder discharge under gravity forming a pile on the bottom of the catching container. The test for each powder was repeated five times, and an average of the obtained angles was considered as a value for the AoR for each powder.

2.3 Discrete element method (DEM)

In DEM, grains, referred to in the following as particles, are treated as rigid bodies, which have translational and rotational degrees of freedom assigned to their center of mass. In this study, the focus is on the behavior of the free-flowing and the dry cohesive powder particles. In the DEM, particle interactions are modeled using the well-established Newton's equations of motion, contact laws and overlap relationships. The soft-particle approach, originally developed by Cundall and Strack [3], is followed in this work, where the particles are allowed to undergo small deformations, i.e., overlaps. Thereafter, these deformations are used to calculate the elastic and plastic deformations besides the frictional forces between the particles [4]. As two particles i and j come in contact with each other, different interactions, i.e., forces and torques due to gravity, deformations under collisions, as well as static and rolling frictions, might occur. Translational and rotational motion of particle i with mass m_i and moment of inertia I_i are represented by the following equations:

Fig. 1 AoR test in two-dimensional CAD view (**a**) and initial laboratory equipment setting (**b**)

$$m_i \frac{d\mathbf{v}_i}{dt} = \sum \left(\mathbf{F}_{ij}^n + \mathbf{F}_{ij}^t \right) + m_i \mathbf{g}, \tag{1}$$

$$I_i \frac{d\boldsymbol{\omega}_i}{dt} = \sum \left(\mathbf{R}_i \times \mathbf{F}_{ij}^t - \boldsymbol{\tau}_{ij}^r \right), \tag{2}$$

where $\mathbf{g}$, $\mathbf{v}_i$ and $\boldsymbol{\omega}_i$ are the gravity vector, translational velocity and rotational velocity of particle i, respectively. The interaction between particle i and j at a defined time step leads to normal and tangential forces, i.e., $\mathbf{F}_{ij}^n$ and $\mathbf{F}_{ij}^t$, respectively. $\mathbf{R}_i$ is the vector between the center of particle i and the contact point, where the tangential force $\mathbf{F}_{ij}^t$ is applied. $\boldsymbol{\tau}_{ij}^r$ is the torque due to rolling friction between the two particles.

2.3.1 Hertz–Mindlin contact model

Hertz–Mindlin [52, 53] contact law is the most common applied approach in modeling contacts between particles. It is used in calculating the contact forces introduced due to the slight considered overlap between particles. The frictional contact force between two granular particles i and j comprises normal $\mathbf{F}_{ij}^n$ and tangential $\mathbf{F}_{ij}^t$ nonlinear contact forces given as

$$\mathbf{F} = \mathbf{F}_{ij}^n + \mathbf{F}_{ij}^t. \tag{3}$$

Each contact force consists of two terms, where the first term stands for the nonlinear elastic Hertz model in the normal direction (spring force) and the linear elastic Mindlin model in the tangential direction (shear force). The second term stands for the damping force (modeled as a dashpot), where a dissipative term is added for both normal and tangential directions to account for energy dissipation during collisions through inelastic deformation and friction. The normal and tangential forces between two spheres i and j during a collision are given by

$$\mathbf{F}_{ij}^n = k_n \boldsymbol{\delta}_{ij}^n - \gamma_n \mathbf{v}_{ij}^n, \tag{4}$$

$$\mathbf{F}_{ij}^t = k_t \boldsymbol{\delta}_{ij}^t - \gamma_t \mathbf{v}_{ij}^t, \tag{5}$$

where k_n and k_t are the elastic constants for the normal and tangential contact, $\boldsymbol{\delta}_{ij}^n$ is the normal contact overlap, given by $|\boldsymbol{\delta}_{ij}^n| = R_i + R_j - l_{ij}$, where l_{ij} is the distance between the centers of the two particles, $\boldsymbol{\delta}_{ij}^t$ is the tangential contact overlap or displacement vector which is truncated to satisfy a frictional yield criterion, given by the integral of the tangential relative velocity through the collision time they are in contact, i.e., $\left| \boldsymbol{\delta}_{ij}^t \right| = \int_0^t \left| \mathbf{v}_{ij}^t \right| dt$, $\mathbf{v}_{ij}^n$ and $\mathbf{v}_{ij}^t$ are the normal and tangential components of the relative velocity of the two particles at the contact, γ_n and γ_t are the viscoelastic damping
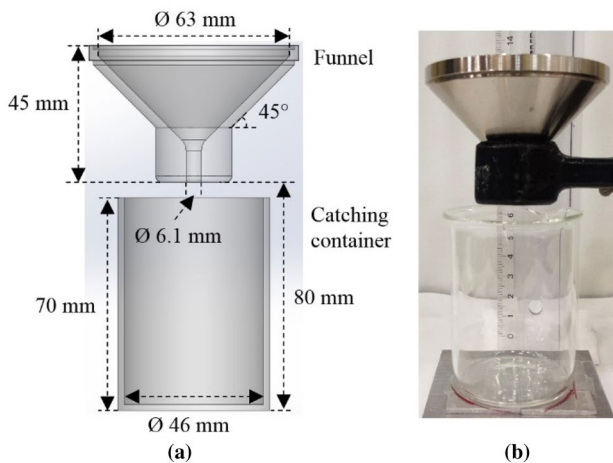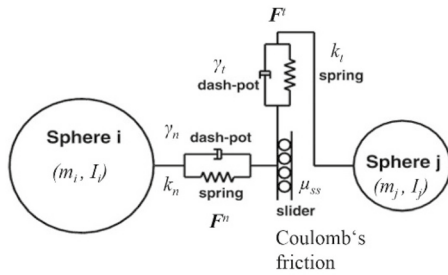
Fig. 2 Schematic representation of the Hertz–Mindlin contact model between particle i and j [54]

constant for normal and tangential contact. Figure 2 illustrates the mechanical system of the interactions of particles in the Hertz–Mindlin contact model.

Under sufficient tangential forces, particles will slip relative to each other or relative to surfaces they are in contact with. For noncohesive particles subjected to a constant normal force, the extent of slippage under tangential force is determined by

$$F_{ij}^t < \mu_{ss}|F_{ij}^n|, \tag{6}$$

where μ_{ss}, represented by a shear slider, is the static friction coefficient between the two particles in the tangential direction. Thus, the tangential force described by a spring and a damper is limited to the Coulomb friction.

Consequently, based on Eqs. (4) and (5), the normal and tangential forces, F_{ij}^n and F_{ij}^t can be expressed in detail as

$$F_{ij}^n = -\frac{4}{3}Y^*\sqrt{R^*\delta_{ij}^n}\delta_{ij}^n - 2\sqrt{\frac{5}{6}}\beta\sqrt{S_n m^*}v_{ij}^n, \tag{7}$$

$$F_{ij}^t = -8G^*\sqrt{R^*\delta_{ij}^n}\delta_{ij}^t - 2\sqrt{\frac{5}{6}}\beta\sqrt{S_t m^*}v_{ij}^t, \tag{8}$$

where Y^* is the equivalent Young's modulus of the two colliding particles. This is defined by $\frac{1}{Y^*} = \frac{1-v_i^2}{Y_i} + \frac{1-v_j^2}{Y_j}$, where v_i and v_j are Poisson's ratios, R^* is the equivalent radius, defined by $\frac{1}{R^*} = \frac{1}{R_i} + \frac{1}{R_j}$, and m^* is the equivalent mass, defined by $\frac{1}{m^*} = \frac{1}{m_i} + \frac{1}{m_j}$. Moreover, $S_n = 2Y^*\sqrt{R^*\delta_{ij}^n}$ and $S_t = 8G^*\sqrt{R^*\delta_{ij}^n}$ are the normal and tangential contact stiffness with G^* being the equivalent shear modulus, defined as $\frac{1}{G^*} = \frac{2(2-v_i)(1+v_i)}{Y_i} + \frac{2(2-v_j)(1+v_j)}{Y_j}$. Besides, β is the damping ratio coefficient, which is a function of the coefficient of restitution, e, and given by $\beta = \ln(e)/\sqrt{\ln^2(e) + \pi^2}$. The coefficient of restitution e is the ratio of relative velocity after collision to the relative velocity before collision. A value of $e = 1$ refers to a perfectly elastic collision, whereas $e = 0$ would mostly be an inelastic collision.

2.3.2 Rolling friction model

In addition to sliding friction, rolling friction is present as a contact-dependent force [55]. Rolling friction is a major parameter that serves as a correction factor by compensating for the use of spherical particle shapes in DEM [56], instead of representing their actual shapes in reality. In the literature, different rolling resistance models have been developed and reviewed [56]. In this work, the alternative elastic–plastic spring-dashpot (EPSD2) rolling resistance model [57], implemented in LIGGGHTS open-source code, is applied to calculate the torque $\tau_{ij,t+\Delta t}^r$ at an incremental time step as

$$\left|\tau_{ij,t+\Delta t}^r\right| \le \mu_r R^*\left|F_{ij}^n\right|, \tag{9}$$

where μ_r is the rolling coefficient. In this model, the damping torque is disabled for simplicity.

2.3.3 Cohesion model

The modified simplified Johnson–Kendall–Roberts cohesion model (SJKR), implemented in LIGGGHTS, is used to model the cohesion of particles. This model originates from the JKR model [58], where it represents the influence of various cohesive forces, such as Van der Waals within the contact zone. It can model high adhesive systems, such as fine and dry powders or wet materials. It adds an additional normal force component F_{coh} to the Hertzian contact law tending to maintain a larger contact area (Fig. 3), i.e.

$$F_{coh} = Ca, \tag{10}$$

where C is the cohesion energy density in J m^{-3} and a is the particle contact area, given as

$$a = \frac{\pi}{4}\frac{(l_{ij} - R_i - R_j) * (l_{ij} + R_i - R_j) * (l_{ij} - R_i + R_j) * (l_{ij} + R_i + R_j)}{l_{ij} * l_{ij}} \tag{11}$$

where R_i and R_j are the radii of sphere i and j, respectively, and l_{ij} is the distance between the particle centers.
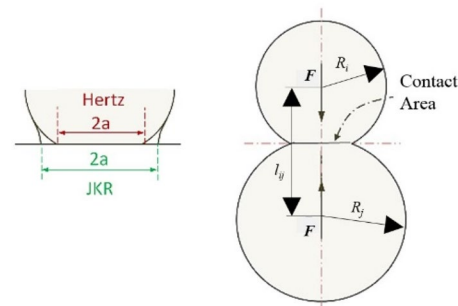

Fig. 3 Schematic representation of the contact area for the JKR model, compared to that of the Hertz model [58]

2.3.4 Noncontact force

In addition to the contact forces, the gravitational acceleration g in the z-direction (with $\hat{z}$ as the unit vector) yields the gravitational force of particle i, $\boldsymbol{F}_i^{\text{grav}}$, which can be expressed as

$$\boldsymbol{F}_i^{\text{grav}} = -m_i g \hat{z}. \tag{12}$$

2.3.5 Time step in DEM simulation

In the DEM simulations of particles flow in this work, the time step (Δt) has been selected to be less than 20% of the critical time step (Rayleigh time) T_R in order to ensure the stability of the integration scheme. T_R is calculated based on the Rayleigh wave propagation, which represents the elastic wave propagation along the surface of one particle to the adjacent contacting particle according to the following equation [59]:

$$\Delta t < T_R = \frac{\pi R \sqrt{\frac{\rho}{G}}}{0.1631\nu + 0.8766}, \tag{13}$$

where ρ is the particle density, G is the shear modulus and ν is the Poisson's ratio.

2.4 Experimental material characterization

This section briefly describes the experimental methods used to find out some material parameters utilized in the DEM simulations. The parameters are divided into two categories: material parameters and interaction parameters [60]. The material parameters include the shape, size, density, elastic and shear modulus as well as Poisson's ratio, whereas the interaction properties are coefficients of restitution, static and rolling frictions and adhesion.

2.4.1 Particle size and shape characterization

Camsizer XT from Retsch Technology GmbH (Germany) was used to measure the volume moment mean (D [3, 4]), which is also called De Brouckere Mean Diameter, and shape of particles via dynamic image analysis. The D [3, 4] indicates around which central point (center of gravity) of the frequency the volume/mass distribution would rotate. The advantage of this method over other particle sizes calculation methods is that it does not require the number of particles in its calculation.

The Camsizer XT helps in approximating the particle shape, where the particles are described in two-dimensional images in terms of the minimum and maximum Feret diameters (Fe_{min}, Fe_{max}). Fe_{min} is the length of the minor axis

and Fe_{max} is the length of the major axis. The ratio of Fe_{min} to Fe_{max} is called the aspect ratio (*ASR*). In this, the aspect ratio with values between 0 and 1 reflects the elongation of a particle and deviation from a sphere where small values correspond to elongated particles and higher values correspond to spherical particles:

$$ASR = \frac{Fe_{min}}{Fe_{max}}. \tag{14}$$

According to Li et al. [61], a shape factor called circularity or roundness (R_o) is an additional factor that indicates to what extent a particle has a spherical shape. It is based on the projected area (A) of the particle and the overall perimeter of the projection (P) according to the following equation:

$$R_o = \frac{4 \times \pi \times A}{P^2}. \tag{15}$$

2.4.2 Density and porosity

The bulk density (BD) and the tapped density (TD) were analyzed via the jolting volumeter (Jel STAV II) from J. Engelsmann AG (Germany). A certain mass of powder was filled into a graduated cylinder, and the volume and mass were then recorded. The test was repeated five times to insure accuracy and repeatability where then an average value was considered. The bulk density represents the average density of the powder sample, where the bulk volume contains voids between individual particles. Therefore, the bulk density of a powder depends on both the material density of the particles and their spatial arrangement. The volume of a bulk solid depends on the size and the shape of the particles. Besides, the tapped density was attained after mechanically compacting the powder sample by up to 1250 taps.

The particle (true) density (ρ_p) was obtained using the Ultrapyc 1200e, Automatic Density Analyzer from Quantachrome Instruments (USA). It is a pycnometer that measures the true density of powder samples using an inert gas (helium) to measure its volume by applying Archimedes' principle of displacement and the technique of gas expansion (Boyle's law). Consequently, the powder bed porosity (ε) is calculated as described in the following equation:

$$\varepsilon = 1 - \frac{BD}{\rho_p} \times 100\%. \tag{16}$$

2.4.3 Carr's index

Based on the BD and TD, powder flowability of bulk solid could be characterized by the Carr's index (CI), or Carr's compressibility index [18]. CI is an indication of the compressibility of a powder, where larger changes indicate poor

flowability [62]. It is a measurement of the relative difference between tapped volume and untapped volume of the powder [47], i.e.

$$CI = \frac{TD - BD}{TD} \times 100\%, \tag{17}$$

Powders with CI < 15% have good flowability, whereas a poor flowability corresponds to CI > 25%.

2.4.4 Cohesion and flow function coefficient

FT4 powder rheometer from Freeman Technology Ltd (UK) was used to find out the cohesion (C) and flowing factor (ff_c) values. A commonly applied approach is the Mohr–Coulomb model that fits the Mohr stress circles to the yield locus that in turns identifies the major principal stress (MPS) and unconfined yield strength (UYS). In this, UYS is related to MPS via the material flow function coefficient ff_c as

$$ff_c = \frac{MPS}{UYS}. \tag{18}$$

Flow function ff_c is commonly used to describe the flowability of a bulk solid. In addition, the cohesion value is identified by the shear cell test [63]. This value is the shear stress at which the normal stress is equal to zero for the best fit of the shear and applied normal stress plot [64]. Generally, a cohesive powder will have higher values for cohesion and UYS and consequently a low ff_c. In particular, ff_c values below 4 denote a very cohesive powder behavior (poor flowing), between 4 and 10 easy-flowing powder and above 10 free-flowing powder.

2.4.5 Static friction

The shear cell test in the FT4 powder rheometer was executed to find out an approximation of the angle of internal friction (AIF) between particles based on the linearized yield locus of the material. It is the angle between the axis of normal stress (abscissa) and the tangent to the yield locus [65]. It measures the shear stress for various normal stresses to describe the magnitude of the shear stress that powder can sustain [65]. From this angle, the interparticle static friction coefficient, denoted by $\mu_{s,pp}$, indicates the resistance between two contacting particles while being sheared [2]. This can be calculated as

$$\mu_{s,pp} = \tan(AIF). \tag{19}$$

2.4.6 Wall friction

The wall friction test, using the FT4 powder rheometer, provides a measurement of the sliding resistance between

the powder and the surface of the process equipment [66]. This test is important for understanding the discharge behavior from a container, especially when using an auger. The measurement principle of a wall friction test is very similar to the shear cell test, where the powder is sheared against a material resembling process equipment wall and not against the powder. The process equipment wall used in this study is a rounded stainless steel disk with 0.05 μm surface roughness. The data from the test are represented as a plot of shear stress against normal stress, allowing to determine the wall friction angle (WFA). It is the arctan of the ratio of the wall shear stress to the wall normal stress [65]. The greater is the wall friction angle, the higher is the resistance between the powder and wall.

Similarly, the coefficient of static friction between a particle and wall ($\mu_{s,pw}$) can be calculated from the wall friction angle as

$$\mu_{s,pw} = \tan(WFA). \tag{20}$$

2.4.7 Moisture content

According to Schulze [18], the holding forces or adhesive forces with the presence of liquid bridges (capillary force) are higher than any other holding forces in bulk materials, as long as the contact distance is very low. The content of moisture sheds the light on some characteristics such as cohesion or agglomeration tendency and can help to describe the flow behavior. The moisture content (MC) was experimentally determined by the halogen drying method using the Halogen Moisture Analyzer type HR73 from Mettler Toledo (USA). A sample amount was heated by a halogen lamp, and thus the moisture is extracted from the powder. Due to this drying process, the bulk loses some weight, and thus the moisture loss is calculated from the difference between the initial and final weights. This moisture loss corresponds to the moisture content of the powder in the initial state.

2.5 Coarse-graining method

To find a trade-off between computational time and accuracy, it is reasonable to limit the number of particles in the DEM simulation. According to Bierwisch et al. [42], coarse-graining (CG) method is a good approach to save significant computational time but DEM simulations with good accuracy are performed in comparison with real tests. In the coarse-graining technique, the original particles with radius R are substituted by larger grains with radius R'. The scaled-up radius R' can be represented as a multiplication of the original grain radius R and a scaling factor S_f. Moreover, CG method is based on an appropriate adjustment of interaction laws and equations of motion according to scaling rules

for the material parameters in such a way that the energy densities, i.e., gravitational potential and kinetic energy, are preserved in the scaled-up system as the original one. As the potential density does not depend on the particle's radius while maintaining a constant volume fraction and particle's density, the particle's density is ought to be fixed upon applying the CG method. According to the coarse-graining proposed by Bierwisch et al. [42], the volume fraction is not affected and, therefore, the potential energy of the scaled system is comparable to the original system. Consequently, the mass of each particle introduced in the system is scaled up by a factor of S_f^3 according to Eq. (21), but as the total number of particles is decreased also by the same factor, the total mass of the particles is conserved:

$$m' = \frac{4}{3}\pi R'^3 \rho' = S_f^3 m. \tag{21}$$

Bierwisch et al. [42] also proved that the energy dissipation per volume and time is preserved if the coefficient of restitution remains the same after applying the coarse-graining method. Thus, the kinetic energy density is preserved because the scaling does not affect particle velocities. In connection with the applied test in this study, i.e., AoR, it is shown that coarse graining has no considerable effect on the resulting angles. In addition, it was observed that the shape of the heap is changing with increasing the particles sizes, where a noticeable tail of the ground heap and a more procumbent peak could be seen for larger particles. Thus, although the CG method leads to highly acceptable results in terms of bulk properties, it is hard to get exactly the same shape of the heap in the DEM simulation after applying the CG method.

2.6 Design of experiment

Design of experiments (DoE) is a systematic technique of planning experiments that is used to determine the cause–effect relationship between factors affecting a process and its responses [67]. It can help in identifying the best combinations of parameters that yield to the desired results and, thus, optimizing the output [32]. The design space of the experiments, in our case simulations, is identified according to the design model used by efficiently selecting the suitable factors combinations to be tested. The DoE method is used to investigate the effects and interactions of DEM input parameters on the output responses, which in turn will facilitate the calibration process. Quadratic D-optimal design model was used to obtain the largest amount of information from the smallest number of simulations using Cornerstone 6.1.1.1 software from camLine GmbH (Germany). The mathematics behind D-optimal design is closely related to the Least Squares method to find the

concrete model equation on the basis of the design and the response data.

2.7 Multivariate regression analysis

Multivariate regression analysis (MVRA) is a statistical technique applied to analyze the variation of more than one outcome variable and thus estimates a regression model. This technique was utilized to observe and analyze the variation and impact of different DEM input parameters on the output parameters. Cornerstone software was used, where the inserted data values are standardized; that is, the original variables are scaled to have a mean of 0 and a variance of 1 as each attribute has a different unit of measurement. The goodness-of-fit of the statistical model was described by the adjusted R^2 (coefficient of determination). R^2 represents the proportion of the variability of the data explained by the model which is adjusted for the number of factors in the model. The confidence level used in the DoE analysis was $\pm 95\%$. An adjusted response graph was used to show the effect of each input parameter on the responses besides showing all data points of the simulation runs, which are not the real measured values but the adjusted ones. The response values are adjusted to average out the effects of the other input parameters. An additional tool in Cornerstone software is the Pareto graph. It expresses the relative size of the effect of each DEM input parameter studied in the model. It shows the orthogonal scaled effects of the factors on the studied responses. To add up, two prediction models based on the regression analysis were built for the sake of predicting an approximate value of the AoR in the free-flowing and cohesive powders.

3 DEM simulations

3.1 Simulation setup

The DEM simulations were performed using the open-source software LIGGGHTS®-Premium 4.X from DCS Computing GmbH (Linz, Austria). The simulations were carried out on an eight-node high-performance cluster using 32 CPUs (Intel Xeon 2.60 GHz). The postprocessing of the simulations was performed using ParaView, version 5.4.1 64-bit from Kitware Inc. (New York, NY, USA). The three-dimensional CAD models used in the DEM simulations were modeled in SolidWorks version Premium 2016 from Dassault Systèmes (Vélizy-Villacoublay, France). After that, the three-dimensional models were meshed using Gmsh, version 3.0.6 [68].

3.2 DEM input parameters

3.2.1 Fixed parameters through the studies

In the DEM simulations, the Hertz–Mindlin contact model and the rolling friction model (EPSD2) were applied for both the free-flowing and the dry cohesive studies. The adhesion contact model (SJKR) was added to the cohesive study. The values of Young's modulus (Y) and the Poisson's ratio (ν) for the funnel and the catching container were selected from the literature [69]. The boundary conditions such as restitution and friction between particle and walls (funnel and glass in this case) were kept constant to reduce the number of simulations in the DoE. Table 1 lists the input parameters in the applied two DEM AoR studies.

3.2.2 Parameters varied in the design of experiments

In the free-flowing study, five particle properties were varied as part of the DoE which were as follows: particle's Young's modulus (Y), particle size (d), coefficient of restitution (e_{pp}), coefficient of static friction ($\mu_{s,pp}$) and coefficient of rolling friction ($\mu_{r,pp}$). In addition to these parameters, cohesion energy density (C_{pp}) was varied in the dry cohesion study. The latter four parameters are related to the particle-to-particle interactions.

In the calibration process, the variation study of the parameters aimed to give the best fit between the DEM simulation and the corresponding reference data. To this end, the $\mu_{s,pp}$ was determined using the FT4 powder rheometer, but because of reducing the Y parameter due to computational limitations, this coefficient was calibrated to get the same bulk solid behavior [45, 70]. e_{pp} and $\mu_{r,pp}$ were also tuned because they are difficult to be determined for microscale powders. When using spherical particle shape, the rolling resistance is considered to be less dominant above the static friction as the contact area is smaller. The range value of the cohesion energy density was roughly estimated by performing presimulation runs or so-called initial screening investigations.

Table 2 lists the values of the six particle properties that were varied in our studies. Three values, which constitute a low, center and high levels for each parameter, were selected. The center values of e_{pp}, $\mu_{s,pp}$, $\mu_{r,pp}$ and C_{pp} are linearly spaced between low and high values, whereas for Y, the center value is spaced on a logarithmic scale. The values of Y in the DoE are logarithmic where the simulation values 0.026, 0.26 and 2.6 GPa are set to 7.41, 8.41 and 9.41 log GPa to ensure a center point in the analysis.

Three-level design was used where each factor was considered at three levels. For the free-flowing powder, 40 simulation runs were executed whereas 53 runs for the dry cohesive one.

Table 1 DEM input parameters considered throughout the two studies

| Material parameter/contact model	Symbol	Unit	Value
Contact model			Hertz–Mindlin
Rolling friction model	EPSD2		Alternative elastic–plastic spring-dashpot model
Cohesion contact model[2]	SJKR		Modified simplified Johnson–Kendall–Roberts model
Young's modulus funnel[1]	Y_F	GPa	200
Young's modulus catching container[1]	Y_C	GPa	67.8
Poisson's ratio funnel[1]	ν		0.28
Poisson's ratio catching container[1]	ν		0.21
Poisson's ratio particle	ν		0.3
Coefficient of restitution particle–wall	e_{pw}		0.2
Coefficient of rolling friction particle–wall	$\mu_{r,pw}$		0.2
Coefficients of restitution and friction wall–wall			0.2
Acceleration due to gravity	g	m/s^2	9.81
Cohesion energy density particle–wall[2]	C_{pw}	J/m^3	1000
Cohesion energy density wall–wall[2]	C_{ww}	J/m^3	100

[1][69]

[2]Set for the cohesion study

Table 2 List of DEM particle input parameters varied in the DoE of the two studies

Material parameter	Symbol	Unit	Value
Young's modulus of particles	Y	GPa	0.026, 0.26, 2.6
Particle diameter of SpheroLac 100	d_S	μm	460, 575, 690
Particle diameter of InhaLac 251	d_I	μm	480.6, 587.4, 694.2
Coefficient of restitution particle–particle	e_{pp}		0.051, 0.3255, 0.6
Coefficient of restitution particle–particle[2]	e_{pp}		0.051, 0.2755, 0.5
Coefficient of static friction particle–particle	$\mu_{s,pp}$		0.1, 0.48, 0.85
Coefficient of static friction particle–particle[2]	$\mu_{s,pp}$		0.2, 0.5, 0.8
Coefficient of rolling friction particle–particle	$\mu_{r,pp}$		0.05, 0.4, 0.75
Coefficient of rolling friction particle–particle[2]	$\mu_{r,pp}$		0.1, 0.4, 0.7
Cohesion energy density particle–particle[2]	C_{pp}	J/m^3	30,000, 50,000, 70,000

[2]Set for the cohesion study
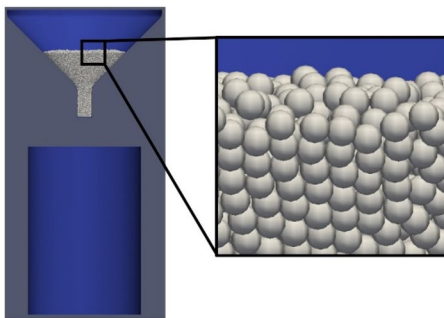
Fig. 4 Initial state of particles filled inside the modified mesh funnel in ParaView software

3.3 DEM studied responses

In preparation of the mesh for the simulations, all the faces that have no contact with the particles were deleted in SolidWorks in order to optimize the computation time. Figure 4 shows the modified mesh file of the funnel in ParaView filled with spherical particles as an initial state before removing the stopper and allowing the particles to flow out.

Five macroscopic output responses, namely AoR, porosity (ε), mass flow rate ($\dot{m}$), overall translational kinetic energy (TKE) and the computation time (CT), on the two powders were studied. The porosity was measured in the funnel due to the simplicity in defining a common volume since no heap (zero AoR) was formed in some simulations. The $\dot{m}$ at the discharge of the funnel was studied, where the mass values were measured every 25 ms. The overall translational kinetic energy (TKE) of the system was calculated over time to check how the dissipation of energy varies according to different simulation input combinations. The average of the TKE, after opening the funnel, was calculated and then normalized (NA-TKE) with the total discharge time of the particles. Table 3 reports the DoE followed and its simulation results of five output responses under the variation in five input parameters for the free-flowing powder.

Table 4 shows the DoE used and the corresponding results of five output responses under the variation in six input parameters for the cohesive powder.

4 Results and discussion

4.1 Material characterization

Table 5 presents the results of the particle size and shape, as well as the bulk properties of the two powders. Based on these material characterization results, the spherical form was selected to represent the particle's shape in LIGGGHTS because both powders have high ASR and R_o values. The values of the ρ_p were used in the DEM setup. The low values of MC in the table prove that both powders are almost dry.

Table 6 lists the flowability values according to Carr's index as well as the shear properties of the two studied powders. The results illustrate how SpheroLac 100 is considered a free-flowing powder because it has low CI, low C and high ff_c. Conversely, InhaLac 251 has high CI, high C and low ff_c values and thus it is considered as a cohesive powder. The values of $\mu_{s,pp}$ were just set as reference values, whereas the values of $\mu_{s,pw}$ were used in the simulation setup.

4.2 Angle of repose experiment

The AoR for each experiment was calculated by taking the average value between the left and right angles, θ_1 and θ_2, respectively. The obtained results of the AoR for both powders were set as reference values in the validation of the regression analysis in the prediction model and thus in the calibration approach. Figure 5 shows the heap formed by the AoR test of the free-flowing powder (SpheroLac 100) in the glass-catching container where the average angle was 33°.

On the contrary, the average AoR of the cohesive powder (InhaLac 251) was 40° where Fig. 6 shows the heap formed in the experiment.

Table 3 Measurements of the five responses, namely AoR, ε, $\dot{m}$, NA-TKE and CT, from the free-flowing DEM simulations

Run	$\mu_{r,pp}$	$\mu_{s,pp}$	e_{pp}	Y (log GPa)	d_S (µm)	AoR (°)	ε (%)	$\dot{m}$ (g/25 ms)	NA-TKE (mJ/s)	CT (hr)
1	0.05	0.1	0.051	7.41	460	15.7	43.37	0.1562	0.28395	3.417
2	0.75	0.1	0.051	7.41	460	18.3	43.65	0.1562	0.27038	3.633
3	0.05	0.85	0.051	7.41	460	17.9	47.47	0.1282	0.19147	3.083
4	0.4	0.48	0.3255	7.41	460	34.2	48.61	0.119	0.15499	3.067
5	0.75	0.1	0.6	7.41	460	0	43.56	0.1562	0.27767	3.117
6	0.05	0.85	0.6	7.41	460	25.5	46.25	0.1316	0.20199	2.486
7	0.75	0.85	0.6	7.41	460	30	49.83	0.1111	0.13257	3.1
8	0.75	0.85	0.051	8.41	460	37.8	52.31	0.1	0.10730	9.717
9	0.05	0.1	0.6	8.41	460	0	43.19	0.1562	0.28704	6.967
10	0.75	0.1	0.051	9.41	460	18	44.32	0.1515	0.26398	21.9
11	0.05	0.85	0.051	9.41	460	18.8	46.99	0.1282	0.18970	31.483
12	0.75	0.85	0.051	9.41	460	37.3	52.35	0.1	0.10924	31.883
13	0.05	0.1	0.3255	9.41	460	11.3	43.42	0.1562	0.28595	27.05
14	0.4	0.1	0.6	9.41	460	0	43.88	0.1562	0.27757	30.367
15	0.75	0.48	0.6	9.41	460	32.8	48.97	0.1163	0.15102	22.583
16	0.05	0.85	0.6	9.41	460	24	46.64	0.1316	0.20092	26.786
17	0.75	0.48	0.051	7.41	575	39	50.99	0.102	0.11446	1.017
18	0.4	0.85	0.3255	7.41	575	35	50.42	0.1064	0.12612	1.05
19	0.4	0.1	0.6	7.41	575	0	44.01	0.1471	0.24504	1.167
20	0.05	0.48	0.3255	8.41	575	24.5	46.65	0.1282	0.18215	4.333
21	0.75	0.1	0.6	8.41	575	0	44.03	0.1471	0.24895	3.53
22	0.05	0.1	0.051	9.41	575	17	44.36	0.147	0.24747	14.733
23	0.75	0.85	0.6	9.41	575	30.2	50.61	0.1064	0.12360	12.983
24	0.05	0.1	0.051	7.41	690	15.8	44.43	0.1429	0.22569	0.645
25	0.05	0.85	0.051	7.41	690	26.5	48.02	0.1163	0.14866	0.65
26	0.75	0.85	0.051	7.41	690	37.5	53.53	0.0887	0.08506	0.883
27	0.75	0.1	0.3255	7.41	690	17	44.39	0.1389	0.22449	0.633
28	0.05	0.1	0.6	7.41	690	0	44.29	0.1429	0.23232	0.486
29	0.75	0.48	0.6	7.41	690	33.5	48.25	0.1064	0.12525	0.5
30	0.05	0.85	0.6	7.41	690	27	46.70	0.119	0.15992	0.65
31	0.75	0.85	0.6	7.41	690	32.3	49.95	0.1	0.10861	0.533
32	0.4	0.1	0.051	8.41	690	18	45.24	0.1776	0.27474	2.283
33	0.4	0.85	0.6	8.41	690	33	50	0.1346	0.15721	2.5
34	0.75	0.1	0.051	9.41	690	18.5	45.42	0.1351	0.20840	5.817
35	0.4	0.48	0.051	9.41	690	34.3	50.47	0.102	0.11600	7.083
36	0.05	0.85	0.051	9.41	690	27.5	48.96	0.1163	0.14799	6.3
37	0.75	0.85	0.3255	9.41	690	35.8	52.59	0.0926	0.09369	5.483
38	0.05	0.1	0.6	9.41	690	0	44.39	0.1388	0.22906	4.967
39	0.75	0.1	0.6	9.41	690	0	45	0.1388	0.22104	5.733
40	0.05	0.85	0.6	9.41	690	25.5	47.40	0.119	0.15692	5.367

4.3 Parametric study

4.3.1 Factors affecting angle of repose

- Free-flowing

The average AoR for each simulation test was calculated. The values of AoR ranged between 0° and 39°, where in eight cases the AoR was equal to zero due to low $\mu_{s,pp}$ as listed in Table 3. Figure 7 presents numerical examples of six AoR DEM simulations for the free-flowing powder formed in the catching container.

The model of the AoR for the free-flowing powder showed an adjusted $R^2 = 0.954$, indicating a very good fit to the data points. Figure 8a shows the adjusted response graph for the AoR. Each of the presented sections (column-wise) corresponds to an input parameter. In each section,

Table 4 Measurements of the five responses, namely AoR, ε, $\dot{m}$, NA-TKE and CT, from the cohesive DEM simulations

Run	$\mu_{r,pp}$	$\mu_{s,pp}$	e_{pp}	Y (log GPa)	d_I (μm)	C_{pp} (J/m^3)	AoR (°)	ε (%)	$\dot{m}$ (g/25 ms)	NA-TKE (mJ/s)	CT (hr)
1	0.7	0.2	0.051	7.41	480.6	70,000	46.7	52.91	0.1263	0.17687	2.483
2	0.1	0.5	0.051	7.41	480.6	70,000	33	53.97	0.1174	0.15372	2.317
3	0.1	0.8	0.051	7.41	480.6	30,000	33.5	53.67	0.1202	0.16813	3.133
4	0.4	0.8	0.2755	7.41	480.6	70,000	43	57.05	0.0965	0.10367	3.133
5	0.7	0.8	0.2755	7.41	480.6	30,000	44	56.79	0.0964	0.10436	3.083
6	0.1	0.2	0.5	7.41	480.6	70,000	35.8	51.20	0.1264	0.18173	3.233
7	0.7	0.2	0.5	7.41	480.6	30,000	41	51	0.1263	0.18733	2.483
8	0.1	0.2	0.051	8.41	480.6	30,000	24.7	50.43	0.1429	0.22378	8.542
9	0.7	0.8	0.051	8.41	480.6	50,000	41.5	57	0.1	0.10710	8.633
10	0.4	0.2	0.5	8.41	480.6	50,000	29.8	50.95	0.1351	0.20982	7.317
11	0.7	0.5	0.5	8.41	480.6	70,000	39	54.51	0.1111	0.13691	7.231
12	0.1	0.8	0.5	8.41	480.6	30,000	31	52.50	0.1282	0.18427	8.455
13	0.1	0.2	0.051	9.41	480.6	70,000	23.5	51.21	0.1413	0.22382	21.85
14	0.7	0.2	0.051	9.41	480.6	30,000	35	51.72	0.1299	0.19235	21.985
15	0.1	0.5	0.051	9.41	480.6	50,000	29.5	52.43	0.1266	0.18295	23.1
16	0.7	0.8	0.051	9.41	480.6	70,000	39	57.06	0.0985	0.10935	22.95
17	0.1	0.8	0.2755	9.41	480.6	30,000	29.2	52.68	0.1267	0.17971	23.217
18	0.1	0.2	0.5	9.41	480.6	30,000	21.7	50.08	0.1412	0.23540	22.833
19	0.7	0.2	0.5	9.41	480.6	70,000	31.5	50.85	0.1232	0.20773	27.05
20	0.1	0.8	0.5	9.41	480.6	70,000	30.5	52.22	0.1266	0.18538	23.35
21	0.7	0.8	0.5	9.41	480.6	30,000	40.5	55.24	0.1072	0.12701	23.12
22	0.7	0.2	0.051	7.41	587.4	30,000	41.5	52.57	0.119	0.15362	1.433
23	0.1	0.5	0.5	7.41	587.4	30,000	31	52.66	0.1219	0.16557	1.1
24	0.4	0.8	0.5	7.41	587.4	50,000	40	56.08	0.1	0.11196	1.267
25	0.7	0.8	0.5	7.41	587.4	70,000	Blocked	–	–	–	–
26	0.7	0.8	0.5	7.41	587.4	30,000	38	56.57	0.098	0.10267	1.283
27	0.1	0.8	0.051	8.41	587.4	70,000	30.8	53.64	0.119	0.15489	3.514
28	0.1	0.2	0.2755	8.41	587.4	70,000	26	51.29	0.1351	0.20434	3.717
29	0.4	0.8	0.051	9.41	587.4	30,000	40	56.50	0.1064	0.12147	14.217
30	0.7	0.5	0.2755	9.41	587.4	50,000	41.5	55.99	0.1042	0.11988	15.767
31	0.1	0.2	0.051	7.41	694.2	50,000	37.5	52.30	0.119	0.15714	0.633
32	0.4	0.5	0.051	7.41	694.2	30,000	40.3	56.53	0.098	0.10468	0.717
33	0.1	0.8	0.051	7.41	694.2	50,000	39.3	54.62	0.1087	0.12998	0.6
34	0.1	0.2	0.051	7.41	694.2	30,000	30	51.62	0.125	0.15372	0.717
35	0.7	0.8	0.051	7.41	694.2	70,000	Blocked	–	–	–	–
36	0.7	0.8	0.051	7.41	694.2	30,000	42	58.89	0.0847	0.07738	0.767
37	0.1	0.2	0.5	7.41	694.2	30,000	27.5	51.05	0.125	0.18082	0.7
38	0.7	0.2	0.5	7.41	694.2	70,000	46	52.35	0.1042	0.11591	0.75
39	0.1	0.8	0.5	7.41	694.2	70,000	36.8	54.01	0.1087	0.13338	0.767
40	0.4	0.2	0.051	8.41	694.2	70,000	34.5	52.66	0.119	0.15716	1.95
41	0.7	0.2	0.2755	8.41	694.2	30,000	37.5	51.50	0.1219	0.16729	1.933
42	0.1	0.8	0.2755	8.41	694.2	30,000	31.5	53.36	0.1136	0.14516	1.967
43	0.1	0.5	0.5	8.41	694.2	70,000	29	52.86	0.119	0.15604	2.03
44	0.7	0.8	0.5	8.41	694.2	30,000	38	55.98	0.0962	0.10210	2.117
45	0.1	0.2	0.051	9.41	694.2	30,000	27	51.40	0.1282	0.17994	8.383
46	0.7	0.2	0.051	9.41	694.2	70,000	32.7	52.51	0.119	0.15717	4.7
47	0.1	0.8	0.051	9.41	694.2	70,000	30.5	54.06	0.1136	0.14289	6.617
48	0.7	0.8	0.051	9.41	694.2	30,000	41	57.84	0.0909	0.09058	5.9
49	0.4	0.5	0.2755	9.41	694.2	70,000	37	54.82	0.1064	0.12178	6.633
50	0.1	0.2	0.5	9.41	694.2	70,000	22.5	51	0.1316	0.19333	6.65

Table 4 (continued)

Run	$\mu_{r,pp}$	$\mu_{s,pp}$	e_{pp}	Y (log GPa)	d_I (μm)	C_{pp} (J/m³)	AoR (°)	ε (%)	$\dot{m}$ (g/25 ms)	NA-TKE (mJ/s)	CT (hr)
51	0.7	0.2	0.5	9.41	694.2	30,000	32.5	51.85	0.125	0.17160	6.883
52	0.1	0.8	0.5	9.41	694.2	30,000	29.5	53.26	0.1163	0.15217	4.983
53	0.7	0.8	0.5	9.41	694.2	70,000	37.5	55.83	0.1	0.10724	6.85

Table 5 Particle size, shape and bulk properties

	D [3, 4] (μm)	ASR	R_o	BD (kg/m³)	TD (kg/m³)	ρ_p (kg/m³)	ε (%)	MC (%)
SpheroLac 100	115		0.746	0.891	758	850	1536.1	50.65	0.08
InhaLac 251	53.4		0.726	0.878	640	891	1539.5	58.43	0.082

Table 6 Flowability and shear properties

	CI (%)	C (kPa) at 6 kPa	ff_c at 6 kPa	AIF (°)	$\mu_{s,pp}$	WFA (°)	$\mu_{s,pw}$
SpheroLac 100	10.82	0.12	20.83	31.38	0.61	6.58	0.115
InhaLac 251	28.18	0.35	7.9	32.68	0.64	6.7	0.117

Fig. 5 Experimental AoR of SpheroLac 100

Fig. 6 Experimental AoR of InhaLac 251

all the data points obtained from simulations are presented in addition to the effect drawn from these points. For a data point, the effects of the other factors included in the model were averaged; therefore, the data points were adjusted in such a way that the effect of the corresponding factor on the response is only presented (adjusted response graph). As the data points were recalculated, it can be seen that the actual values of the responses listed in Table 3 do not match with the adjusted values, yet the effect of each parameter can still be modeled. Finally, scattering points signify data points that cannot be described by the model due to some noise effects.

From Fig. 8a, the following trends can be observed regarding AoR: Y and d_S have no significant effects on the AoR, e_{pp} and $\mu_{r,pp}$ have a slight effect and $\mu_{s,pp}$ has the major effect. The absence of d_S as an effective factor to the AoR ensures the correct implementation of the coarse-graining scheme proposed by Bierwisch in our system. Moreover,

our results contradict many studies which proved that the particle size has an impact on the AoR [22, 25, 47].

Figure 9 illustrates the Pareto graph of effects on the AoR of the free-flowing powder where the largest positive effects are shown on the left and the largest negative effects on the right, with factors of smaller estimated effects in the middle of the graph. It can be seen that $\mu_{s,pp}$ has the highest positive effect (proportional) on the AoR, where, as $\mu_{s,pp}$ increases, the AoR increases as well. The rest of the affecting factors, i.e., $\mu_{r,pp}$ and e_{pp}, interactions (e.g., $\mu_{s,pp} * \mu_{r,pp}$), and quadratic terms (e.g., e_{pp}^2) have lower effect compared to that of $\mu_{s,pp}$. To be stated, as e_{pp} increases, the AoR decreases, which is previously confirmed by Wei et al. [35]. As e_{pp} is the ratio of the relative velocity after collision to the relative velocity before collision of an object with a surface, the results can be explained by the fact that due to the high elasticity of the spherical particles, they can more likely bounce than to settle down along a free surface.

- Cohesive

Figure 10 illustrates numerical examples of six AoR DEM simulations for the cohesive powder formed in the catching container.

The adjusted R^2 of the AoR of the cohesive powder model has a very good value of 0.915. Figure 11a shows the adjusted response graph for the AoR. It indicates that the introduction of cohesion in the system through the SJKR model added a new affecting parameter on the AoR, which is Y. Unlike the free-flowing case, it is proved that Y has a significant negative effect on AoR when C_{pp} is involved. This ensures the importance of such a parametric study, where Y is not included in many other calibration processes
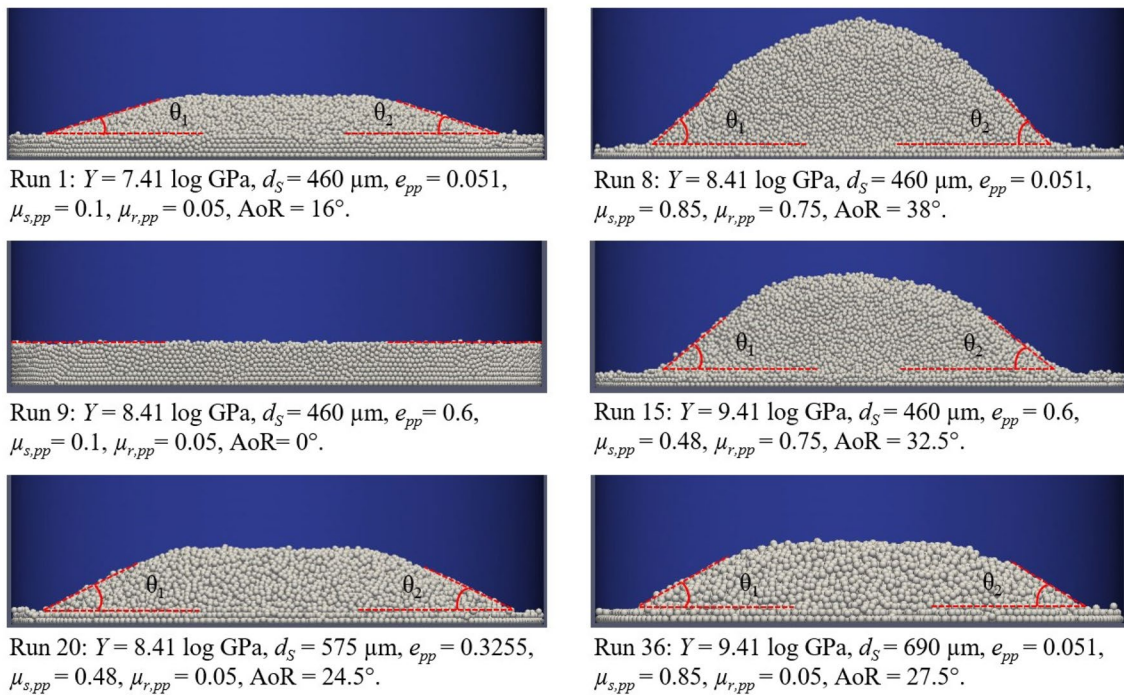
Run 1: Y = 7.41 log GPa, d_S = 460 μm, e_{pp} = 0.051, $\mu_{s,pp}$ = 0.1, $\mu_{r,pp}$ = 0.05, AoR = 16°.

Run 8: Y = 8.41 log GPa, d_S = 460 μm, e_{pp} = 0.051, $\mu_{s,pp}$ = 0.85, $\mu_{r,pp}$ = 0.75, AoR = 38°.

Run 9: Y = 8.41 log GPa, d_S = 460 μm, e_{pp} = 0.6, $\mu_{s,pp}$ = 0.1, $\mu_{r,pp}$ = 0.05, AoR = 0°.

Run 15: Y = 9.41 log GPa, d_S = 460 μm, e_{pp} = 0.6, $\mu_{s,pp}$ = 0.48, $\mu_{r,pp}$ = 0.75, AoR = 32.5°.

Run 20: Y = 8.41 log GPa, d_S = 575 μm, e_{pp} = 0.3255, $\mu_{s,pp}$ = 0.48, $\mu_{r,pp}$ = 0.05, AoR = 24.5°.

Run 36: Y = 9.41 log GPa, d_S = 690 μm, e_{pp} = 0.051, $\mu_{s,pp}$ = 0.85, $\mu_{r,pp}$ = 0.05, AoR = 27.5°.
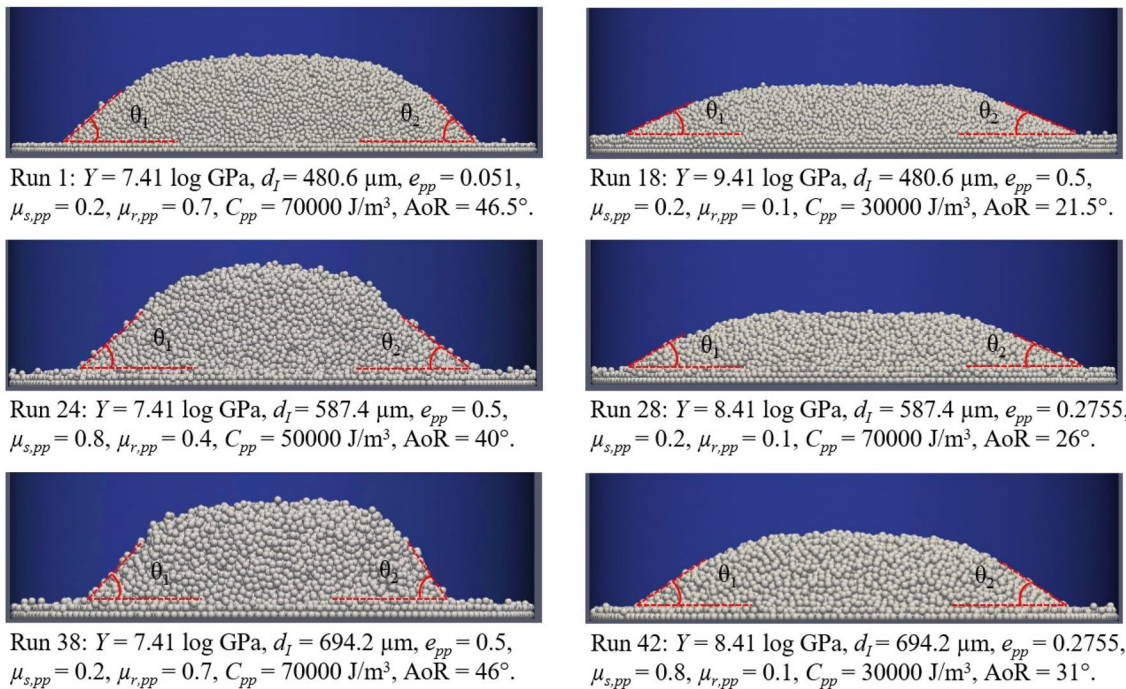
Fig. 7 Illustration of AoR of six different DEM run conditions of the free-flowing powder
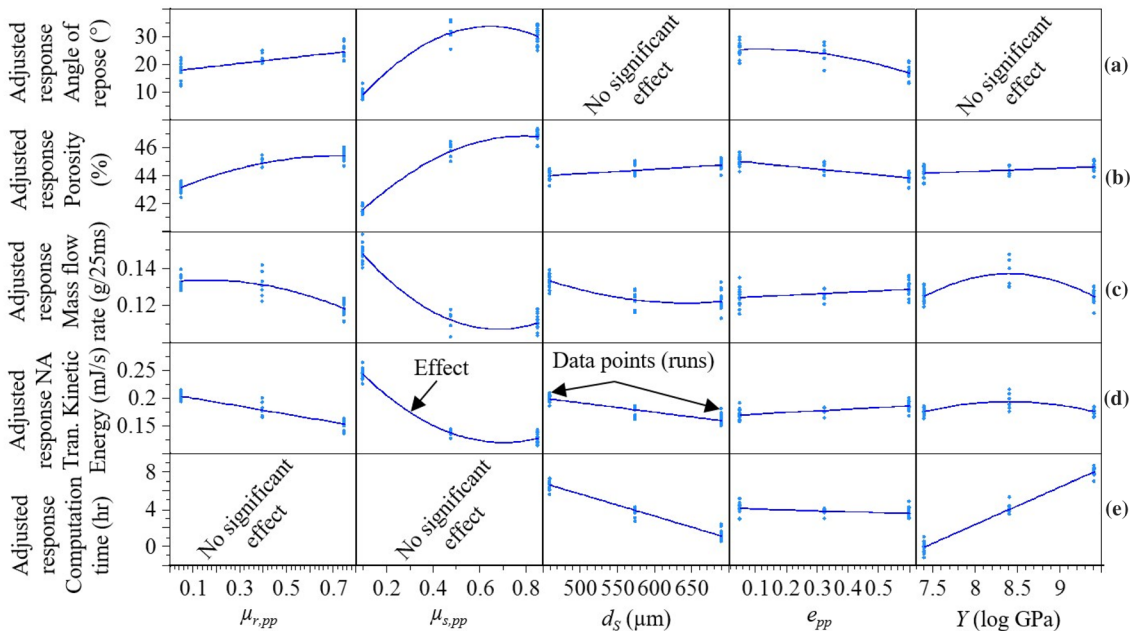
Fig. 8 Adjusted response graph of the **a** AoR, **b** ε, **c** ṁ, **d** NA-TKE and **e** CT for the free-flowing as in relation to the five varied DEM input parameters

due to its computational cost impact, though it has influence. From Fig. 11a, it can be seen that the angle of repose increases with an increase in the sliding and rolling friction coefficients, which is proven in other studies as well [25, 46, 71–74]. This positive correlation is similar in both free-flowing and cohesive powders.

Figure 12 demonstrates the Pareto graph of effects on the AoR of the cohesive powder. It shows that $\mu_{r,pp}$ has the
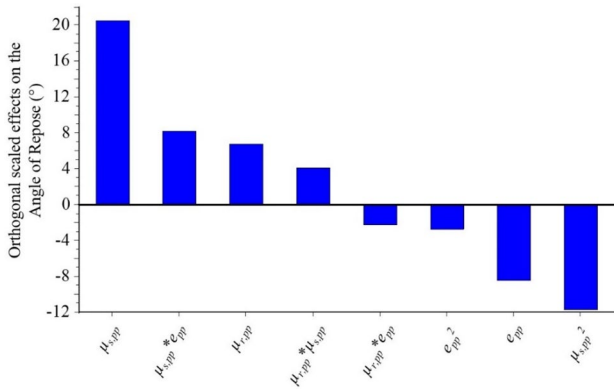
Fig. 9 Pareto graph of effects of the model factors on the AoR of the free-flowing powder

highest positive effect on the AoR, which is contrary to most of the studies that proved the superiority of $\mu_{s,pp}$ in terms of effectivity. Therefore, it is very critical to always relate the effectiveness of the parameters to the circumference of the case study. Moreover, Y has a bigger impact on the AoR than $\mu_{s,pp}$.

4.3.2 Factors affecting porosity

- Free-flowing

The regression analysis of the ε of the free-flowing powder resulted in a very good adjusted R^2 value of 0.981. The

adjusted response graph of ε in Fig. 8b demonstrates the high significance positive correlation of $\mu_{s,pp}$ on ε followed with $\mu_{r,pp}$, which was also proven by Wei et al. [35]. The other studied microscopic parameters indicated less significance, where the relative size of effects of these parameters is presented in Fig. 13.

- Cohesive

The adjusted R^2 of the ε of the cohesive powder was very good as well with a value of 0.983. Similarly to the free-flowing powder, $\mu_{s,pp}$ had the highest positive influence on ε followed with $\mu_{r,pp}$ as revealed in Fig. 11b. In addition, the Pareto graph of effect in Fig. 14 shows the superiority positive relative effect of $\mu_{s,pp}$ on ε compared to the other parameters.

4.3.3 Factors affecting mass flow rate

- Free-flowing

The adjusted R^2 of the $\dot{m}$ model of the free-flowing powder was recorded to be 0.95. The adjusted response graph for the $\dot{m}$ is shown in Fig. 8c. As observed, all the studied parameters affect the $\dot{m}$, but each in a different way which is also presented in the Pareto graph (Fig. 15). The Pareto graph shows that $\mu_{s,pp}$ has the highest negative effect on the $\dot{m}$. This indicates that as $\mu_{s,pp}$ increases, the particles' flow out of the funnel gets delayed due to the sliding friction

Run 1: $Y = 7.41$ log GPa, $d_I = 480.6$ μm, $e_{pp} = 0.051$, $\mu_{s,pp} = 0.2$, $\mu_{r,pp} = 0.7$, $C_{pp} = 70000$ J/m³, AoR = 46.5°.

Run 18: $Y = 9.41$ log GPa, $d_I = 480.6$ μm, $e_{pp} = 0.5$, $\mu_{s,pp} = 0.2$, $\mu_{r,pp} = 0.1$, $C_{pp} = 30000$ J/m³, AoR = 21.5°.

Run 24: $Y = 7.41$ log GPa, $d_I = 587.4$ μm, $e_{pp} = 0.5$, $\mu_{s,pp} = 0.8$, $\mu_{r,pp} = 0.4$, $C_{pp} = 50000$ J/m³, AoR = 40°.

Run 28: $Y = 8.41$ log GPa, $d_I = 587.4$ μm, $e_{pp} = 0.2755$, $\mu_{s,pp} = 0.2$, $\mu_{r,pp} = 0.1$, $C_{pp} = 70000$ J/m³, AoR = 26°.

Run 38: $Y = 7.41$ log GPa, $d_I = 694.2$ μm, $e_{pp} = 0.5$, $\mu_{s,pp} = 0.2$, $\mu_{r,pp} = 0.7$, $C_{pp} = 70000$ J/m³, AoR = 46°.

Run 42: $Y = 8.41$ log GPa, $d_I = 694.2$ μm, $e_{pp} = 0.2755$, $\mu_{s,pp} = 0.8$, $\mu_{r,pp} = 0.1$, $C_{pp} = 30000$ J/m³, AoR = 31°.

Fig. 10 Illustration of AoR of six different DEM run conditions of the cohesive powder
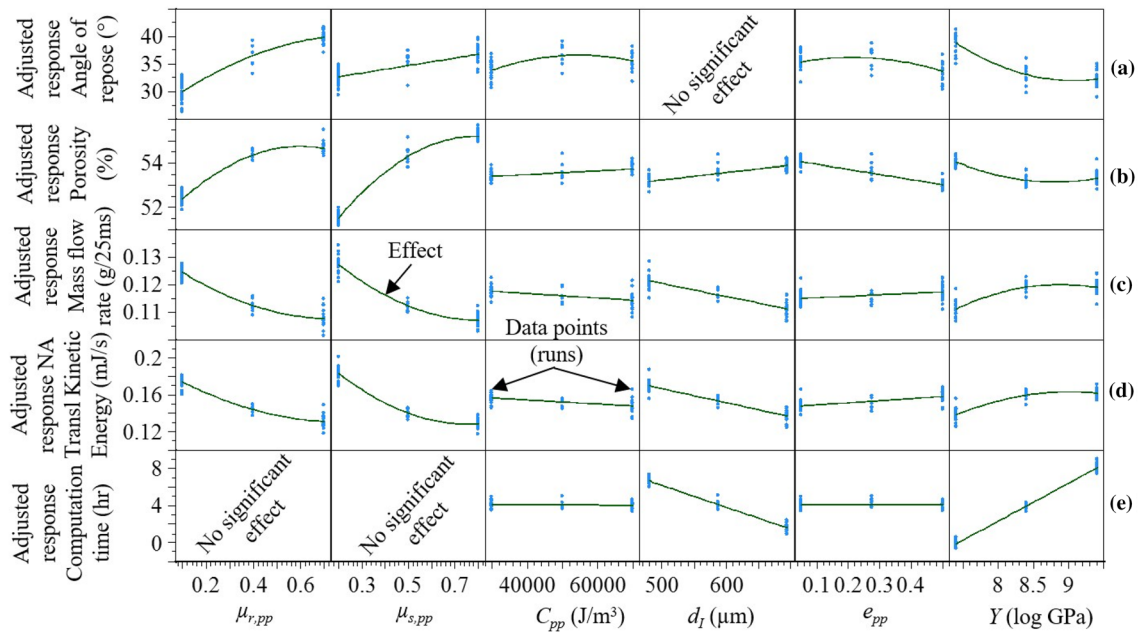
Fig. 11 Adjusted response graph of the **a** AoR, **b** ε, **c** $\dot{m}$, **d** NA-TKE and **e** CT for the cohesive as in a relation to the six varied DEM input parameters
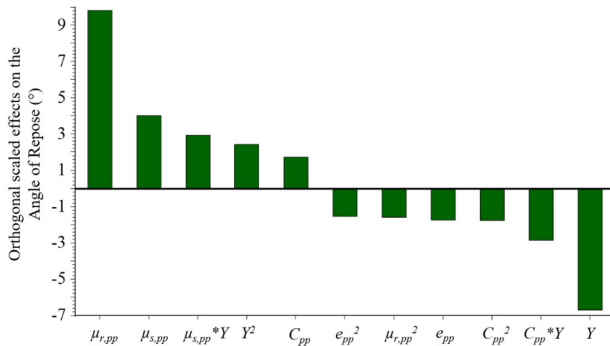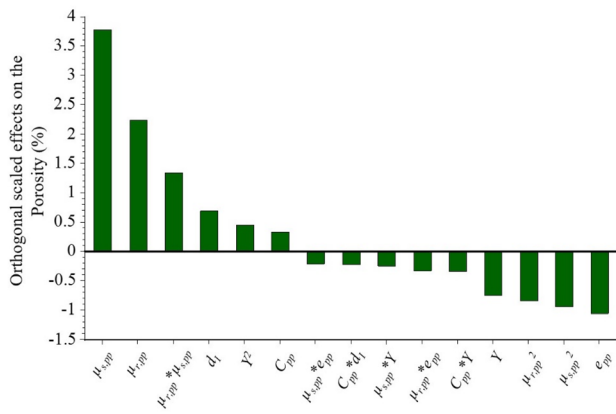

Fig. 12 Pareto graph of effects of the model factors on the AoR of the cohesive powder
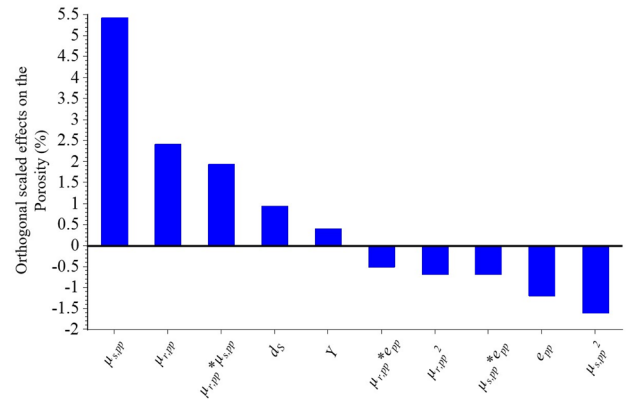
**Fig. 13** Pareto graph of effects of the model factors on the ε of the free-flowing powder

between the particles. The same holds for $\mu_{r,pp}$ and d_S. Unlike e_{pp}, as it increases, $\dot{m}$ increases slightly.

Following this, the mass and $\dot{m}$ of the six example simulations shown in Fig. 10 were plotted over time in one graph (Fig. 16) to compare them with each other. The parameter combinations and the mean $\dot{m}$ values of each run are presented in Table 3.

Figure 16 shows that the slopes of mass graphs M_1 and M_9, corresponding to the first and ninth DEM simulations, have the highest $\dot{m}$ while having the lowest values of $\mu_{s,pp}$

(0.1). M_8 is showing the lowest slope ($\dot{m}$) with the assignment of having a high value of $\mu_{s,pp}$ (0.85).

- Cohesive

The model fit of the $\dot{m}$ in the cohesive study was very good with an adjusted $R^2 = 0.957$. Figure 11c presents the adjusted response graph for the $\dot{m}$, and the Pareto graph (Fig. 17) shows the weight value effect of the input

Fig. 14 Pareto graph of effects of the model factors on the ε of the cohesive powder
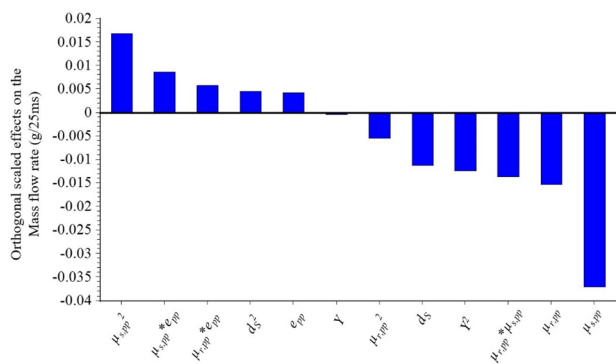
Fig. 15 Pareto graph of effects of the model factors on the $\dot{m}$ of the free-flowing powder
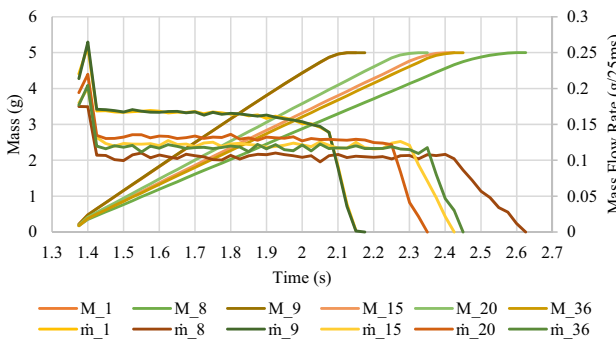
Fig. 16 Mass and $\dot{m}$ over time of six DEM simulations of the free-flowing powder

parameters on the $\dot{m}$. It is apparently shown that $\dot{m}$ has been highly negatively affected by $\mu_{s,pp}$, $\mu_{r,pp}$ and d_I in decreasing order of effectivity. A lower but significant positive effect has been witnessed for Y. This is due to the fact that particles with high stiffness tend to flow easier under the effect of gravity.
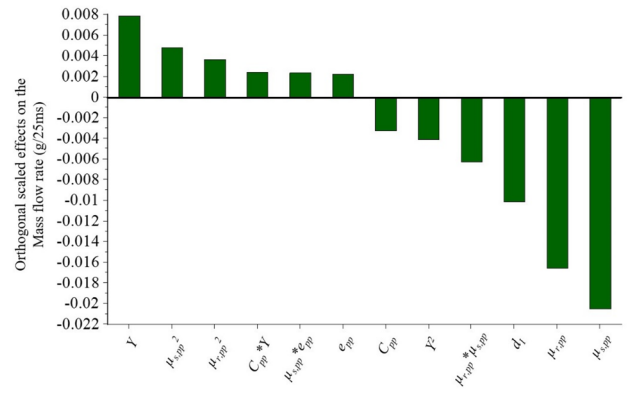
Fig. 17 Pareto graph of effects of the model factors on the $\dot{m}$ of the cohesive powder
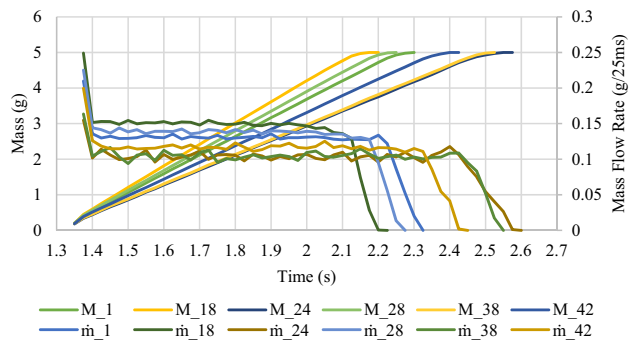
Fig. 18 Mass and $\dot{m}$ over time of six DEM simulations of the cohesive powder

More clear visualization of how $\dot{m}$ is varying with respect to the parameters can be seen in Fig. 18, which shows an example of the mass and $\dot{m}$ of six simulation cases plotted over time. The varied input parameters and the mean $\dot{m}$ values of each run are presented in Table 4.

4.3.4 Factors affecting kinetic energy

- Free-flowing

The overall translational kinetic energy (TKE) was recorded every 1 ms starting from the moment of particle insertion inside the funnel till the discharge of the last particle inside the catching container. The results showed that $\mu_{s,pp}$ has a negative impact on the TKE as illustrated in an example of three runs in Fig. 19.

From 0 to 1 s, the particles were inserted inside the funnel, and then there was 0.3 s settlement time for the particles before removing the stopper at 1.3 s. This resulted in having an almost identical character of variation of TKE from 0 to 1.3 s. The rapid increase in TKE within 0–0.1 s is explained by the falling (insertion) of the particles into the funnel.

Within 0.1–1 s, the distance between the insertion region and the first contact of the particles in the vertical direction decreased as the funnel was being filled with particles. Then, as the particles were settling down, the TKE started decreasing. In the time between 1 and 1.3 s, a rapid decrease in the TKE was observed as no more particles are inserted and most of the particles are got in rest (settled down). It can be seen that upon removing the stopper, the peak of $E_{kin\_}7$ was smaller than that of $E_{kin\_}5$ and then $E_{kin\_}7$ remained smaller and the total time for full discharge was longer compared to $E_{kin\_}5$. The only difference between these two runs is the value of the $\mu_{s,pp}$ where it was 0.1 in run 5 and 0.85 in run 7. So, the high value of $\mu_{s,pp}$ decreases the overall TKE of the system.

On the other hand, $E_{kin\_}2$ has a smaller e_{pp} than $E_{kin\_}5$ which showed a minimal difference in a small interval of time during the discharge of the particles. Thus, e_{pp} has no significant influence on the overall TKE when $\mu_{s,pp}$ is low. On the contrary, e_{pp} has a significant influence on the overall TKE when $\mu_{s,pp}$ and $\mu_{r,pp}$ are both high as shown in Fig. 20.

Moreover, the particle size d_S has a major influence on the overall TKE. Figure 21 plots the overall TKE graphs of simulation cases 1 and 24 where the d_S in run 1 is 460 μm and the d_S in run 24 is 690 μm.

The graph plot shows that both runs have similar overall TKE during the insertion time. After removing the stopper, the overall TKE of run 1 with lower d_S (460 μm) is higher and reaches full discharge faster than run 24 with higher d_S (690 μm). This can be explained by that the number of particles decreases with the increase in radii keeping the same mass; therefore, the number of collisions decreases and thus leads to a decrease in the TKE.

For a better understanding of the relative level of effectivity of these parameters, the adjusted response graph and Pareto chart are also designed for this response. The adjusted R^2 of the NA-TKE model of the free-flowing powder was 0.981. In Fig. 8d, the adjusted response graph for the NA-TKE is illustrated. The Pareto graph of effects on the

NA-TKE of the free-flowing powder is shown in Fig. 22. It shows that the quadratic term of $\mu_{s,pp}$ has the highest positive effect and $\mu_{s,pp}$ has the highest negative effect on the NA-TKE, followed by $\mu_{r,pp}$. This result harmonizes perfectly with the definitions of these two factors, as they represent, more or less, the extent of resistance of a particle to remain in its position upon being exposed to a certain force. Therefore, as they increase, the particles are more hindered, and therefore the TKE decreases. And since the particles in our system do not tend to move in the rotational direction as in the translational direction, the $\mu_{r,pp}$ is showing less effect than $\mu_{s,pp}$.

- Cohesive

The model fit of the NA-TKE of the cohesive powder was very good with an adjusted $R^2 = 0.97$. The adjusted response graph for the NA-TKE is shown in Fig. 11d. The Pareto graph of effects on the NA-TKE (Fig. 23) shows that Y has the highest positive effect and $\mu_{s,pp}$ has the highest negative effect on the NA-TKE. As seen, a new factor, namely Y, compared to the free-flowing case, has been introduced as a significant parameter. The reason for that is the existence of the C_{pp} in the system representing an additional normal contact force tending to stick the particles more to each other. As Y denotes the stiffness of the particles, exerting an
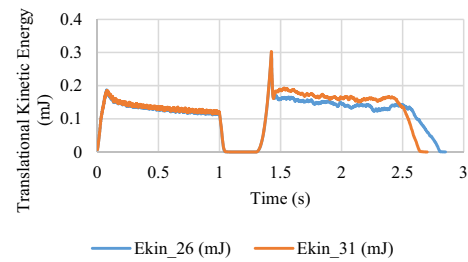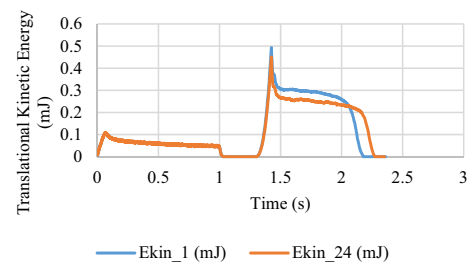

Fig. 20 Overall TKE graph plot over time for simulation runs 26 and 31 for the free-flowing powder. Conditions for these plots: $\mu_{r,pp}=0.75$, $\mu_{s,pp}=0.85$, $Y=7.41$ log GPa, $d_S=690$ μm, $e_{pp}=0.051$ ($E_{kin\_}26$) and $e_{pp}=0.6$ ($E_{kin\_}31$)

Fig. 19 Overall TKE graph plot over time for simulation runs 2, 5 and 7 for the free-flowing powder. Conditions for these plots: $\mu_{r,pp}=0.75$, $Y=7.41$ log GPa, $d_S=460$ μm, $e_{pp}=0.6$ ($E_{kin\_}5$ and $E_{kin\_}7$), $e_{pp}=0.051$ ($E_{kin\_}2$), $\mu_{s,pp}=0.1$ ($E_{kin\_}2$ and $E_{kin\_}5$) and $\mu_{s,pp}=0.85$ ($E_{kin\_}7$)

Fig. 21 Overall TKE graph plot over time for simulation runs 1 and 24 for the free-flowing powder. Conditions for these plots: $\mu_{r,pp}=0.05$, $\mu_{s,pp}=0.1$, $e_{pp}=0.051$, $Y=7.41$ log GPa, $d_S=460$ μm, ($E_{kin\_}1$) and $d_S=690$ μm ($E_{kin\_}24$)
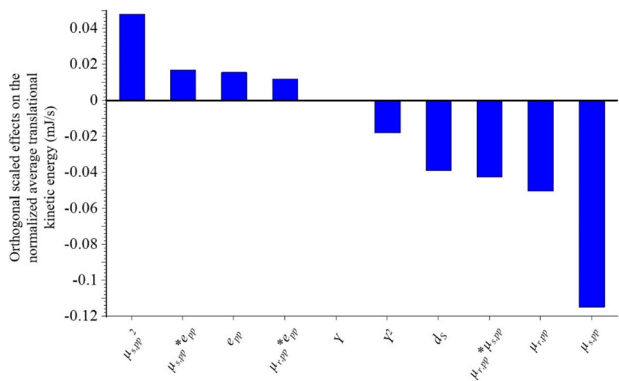
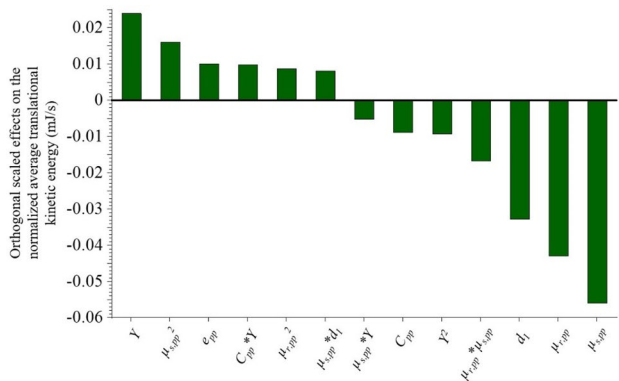Fig. 22 Pareto graph of effects of the model factors on the NA-TKE of the free-flowing powder

Fig. 23 Pareto graph of effects of the model factors on the NA-TKE of the cohesive powder
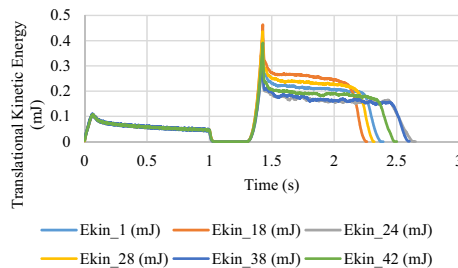

Fig. 24 Overall TKE graph plot over time for simulation runs 1, 18, 24, 28, 38 and 42 for the cohesive powder
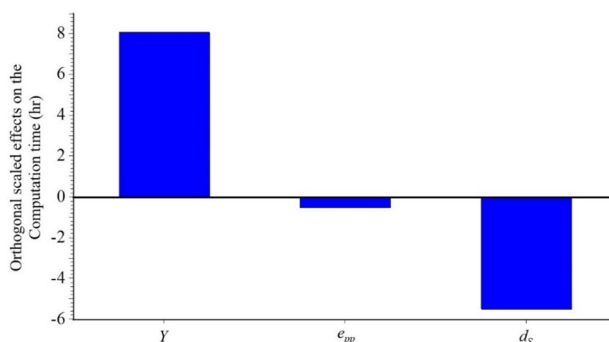

Fig. 25 Pareto graph of effects of the model factors on the CT of the free-flowing powder

4.3.5 Factors affecting computation time

- Free-flowing

The CT model of the free-flowing powder had a very high adjusted R^2 value of 0.987. It is clearly shown in Table 3 how the CT is varying through the different simulation runs. The adjusted response graph for the CT is illustrated in Fig. 8e. In addition, Fig. 25 demonstrates the Pareto graph of effects on the CT of the free-flowing powder. It is indicated that Y has a big positive impact on CT, whereas d_S has a smaller negative effect on it. In other words, as the Y becomes bigger, the CT increases and as d_S increases, the CT decreases. Although e_{pp} has much less effect on CT compared to Y and d_S, yet it is important to notice that e_{pp} has a negative effect which might be used in another applications needing relatively high computation time.

- Cohesive

The adjusted R^2 of the CT model of the cohesive powder was very high as well (0.991). Figure 11e illustrates the adjusted response graph for the CT, and Fig. 26 presents the Pareto graph of effects on the CT of the cohesive powder. Similarly, the results showed that Y and d_I are the almost

additional force on them along with less tendency to deform leads to some repulsion causing the higher velocity of the particles. This interactive effect of these two parameters can be seen also by the term $C_{pp} * Y$ having a positive impact on the NA-TKE. On the contrary, maintaining the same value of Y with increasing the C_{pp}, decreases the NA-TKE, because the additional normal contact force ought to keep the particles in contact. It can be also observed that the particle size has a higher significant effect than in the free-flowing case. In fact, this can be justified by the increase in contact area along with the increase in normal contact force, the thing that would cause an increase in the frictional force in order to maintain a constant $\mu_{s,pp}$.

In Fig. 24, the overall behavior of the TKE of the system in the cohesive case generally looks similar to the free-flowing case. Some phenomena discussed earlier regarding the effects of some parameters can be seen.
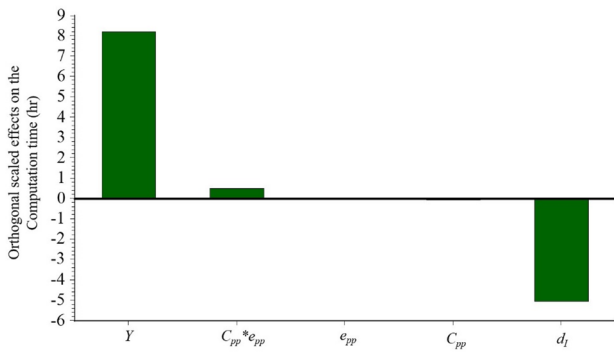
Fig. 26 Pareto graph of effects of the model factors on the CT of the cohesive powder

only two parameters affecting the CT as in the free-flowing study. In that, using a small Y and bigger d, via coarse-graining method, would save a lot of computational costs.

To add up, the count of particles for the free-flowing powder was 18,923, 32,700 and 63,864 when using particle size values of 690 μm, 575 μm and 460 μm, respectively, after applying CG. On the other side, the number of particles for the cohesive powder was 18,540, 30,604 and 55,877 when using particle size values of 694.2 μm, 587.4 μm and 480.6 μm, respectively.

Table 7 sums up the adjusted R^2 values of the regression models of the five responses on the free-flowing and cohesive powders.

4.4 Prediction model and experimental validation

The main aim of this section is to validate the regression models of the parametric studies obtained above and to validate the numerical model based on experimental data. Therefore, the reference values of the AoR and ε determined from the experiments will be our targets in the following prediction simulations.

4.4.1 Free-flowing

Based on the results obtained, a prediction model was built to estimate the AoR and ε upon using an optimized combination between them. The predicted AoR and ε for the free-flowing powder are calculated according to Eqs. (22) and (23), respectively, as follows:

$$
\begin{aligned}
\text{AoRS} = {} & \lambda + \lambda_1 \cdot e_{\text{pp}} + \lambda_2 \cdot \mu_{\text{s,pp}} + \lambda_3 \cdot \mu_{\text{r,pp}} \\
& + \lambda_4 \cdot \mu_{\text{r,pp}} \cdot \mu_{\text{s,pp}} + \lambda_5 \cdot \mu_{\text{r,pp}} \cdot e_{\text{pp}} \\
& + \lambda_6 \cdot \mu_{\text{s,pp}} \cdot e_{\text{pp}} + \lambda_7 \cdot \mu_{\text{s,pp}}^2 + \lambda_8 \cdot e_{\text{pp}}^2,
\end{aligned}
\tag{22}
$$

Table 7 Summary of the adjusted R^2 values of the ten regression models

	Free-flowing					Cohesive				
	AoR	ε	ṁ	NA-TKE	CT	AoR	ε	ṁ	NA-TKE	CT
Adjusted R^2	0.954	0.981	0.95	0.981	0.987	0.915	0.983	0.957	0.97	0.991

Table 8 Factors of the prediction model equations of the AoR and the ε for the free-flowing and cohesive powders

Variable	Factors of AoR (free-flowing)	Factors of ε (free-flowing)	Factors of AoR (cohesive)	Factors of ε (cohesive)
λ	6.7266	37.9127	202.481	73.8381
λ_1	−5.9508	0.0041	30.4258	8.1474
λ_2	87.8684	0.2037	−34.8184	17.7210
λ_3	6.0857	0.4985	13.1172	−0.5760
λ_4	15.6309	16.2729	−43.4370	−7.4100
λ_5	−11.8716	5.3753	0.0010	0.0058
λ_6	39.7847	7.38747	4.9399	0.0001
λ_7	−83.8815	−2.6774	−7.1505e−05	7.5073
λ_8	−36.3797	−3.4024	−17.5265	−2.4609
λ_9	–	−5.6972	−30.8083	−1.5762
λ_{10}	–	−11.4497	2.4489	−0.4159
λ_{11}	–	–	−4.4295e−09	−8.7405e−06
λ_{12}	–	–	–	−5.2809e−08
λ_{13}	–	–	–	−9.3584
λ_{14}	–	–	–	−10.4861
λ_{15}	–	–	–	0.4565

$$\varepsilon S = \lambda + \lambda_1 \cdot d_S + \lambda_2 \cdot Y + \lambda_3 \cdot e_{pp} + \lambda_4 \cdot \mu_{s,pp}$$
$$+ \lambda_5 \cdot \mu_{r,pp} + \lambda_6 \cdot \mu_{r,pp} \cdot \mu_{s,pp} + \lambda_7 \cdot \mu_{r,pp} \cdot e_{pp} \qquad (23)$$
$$+ \lambda_8 \cdot \mu_{s,pp} \cdot e_{pp} + \lambda_9 \cdot \mu_{r,pp}^2 + \lambda_{10} \cdot \mu_{s,pp}^2$$

The constants in both equations are presented in Table 8.

As the value 0.61, which represents the experimental value of $\mu_{s,pp}$ of the free-flowing powder using the FT4 rheometer, is within the tested range of $\mu_{s,pp}$, it was fixed in the prediction model. In addition, according to the obtained results, Y was set to minimum and d_S was set to maximum to reduce the CT. Using an integrated optimization feature algorithm in Cornerstone software, an optimized DEM parameter combination of $\mu_{r,pp}$ and e_{pp}, which aims to match our studied bulk responses (AoR and ε) with the experimental reference values with minimum deviation errors, is selected. Table 9 shows the combination of the DEM input parameters used in validating the prediction model and thus calibrating SpheroLac 100 (the free-flowing) with its experimental AoR and ε values. The values to be predicted were set as our experimental reference values.

The results in Table 9 validate the robustness of our regression model, and thus our powder was calibrated. On this occasion, Fig. 27 shows the numerical AoR of run 41 validated with the experimental AoR of the free-flowing powder.

4.4.2 Cohesive

Similarly, Eqs. (24) and (25) represent the prediction equations for the AoR and ε for the cohesive powder, respectively, as follows:

$$AoRI = \lambda + \lambda_1 \cdot \mu_{r,pp} + \lambda_2 \cdot \mu_{s,pp} + \lambda_3 \cdot e_{pp}$$
$$+ \lambda_4 \cdot Y + \lambda_5 \cdot C_{pp} + \lambda_6 \cdot \mu_{s,pp} \cdot Y$$
$$+ \lambda_7 \cdot C_{pp} \cdot Y + \lambda_8 \cdot \mu_{r,pp}^2 + \lambda_9 \cdot e_{pp}^2 + \lambda_{10} \cdot Y^2 + \lambda_{11} \cdot C_{pp}^2, \quad (24)$$

$$\varepsilon I = \lambda + \lambda_1 \cdot \mu_{r,pp} + \lambda_2 \cdot \mu_{s,pp} + \lambda_3 \cdot e_{pp} + \lambda_4 \cdot Y + \lambda_5 \cdot d_I$$
$$+ \lambda_6 \cdot C_{pp} + \lambda_7 \cdot \mu_{r,pp} \cdot \mu_{s,pp} + \lambda_8 \cdot \mu_{r,pp} \cdot e_{pp}$$
$$+ \lambda_9 \cdot \mu_{s,pp} \cdot e_{pp} + \lambda_{10} \cdot \mu_{s,pp} \cdot Y + \lambda_{11} \cdot C_{pp} \cdot Y$$
$$+ \lambda_{12} \cdot C_{pp} \cdot d_I + \lambda_{13} \cdot \mu_{r,pp}^2 + \lambda_{14} \cdot \mu_{s,pp}^2 + \lambda_{15} \cdot Y^2. \qquad (25)$$

The constants of these latter equations are listed in Table 8 as well. To be stated, the prediction equations for both free-flowing and cohesive powders showed a nonlinear relation between the parameters, unlike the study conducted by Boikov [75]. He had no ambiguity in his sought responses as he assumed that the parameters are linearly dependent. It
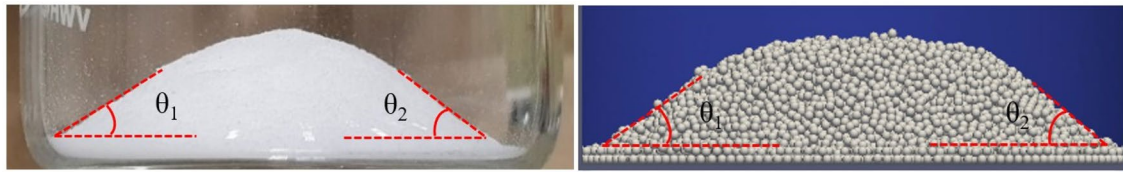
Table 9 Executed simulation run for the validation of the process model of the AoR and the ε of the free-flowing powder

Run	$\mu_{r,pp}$	$\mu_{s,pp}$	e_{pp}	Y (log GPa)	d_S (μm)	Predicted AoR (°)	DEM AoR (°)	Deviation error of AoR (%)	Predicted ε (%)	DEM ε (%)	Deviation error of ε (%)
41	0.58	0.61	0.566	7.41	690	33	33.4	+1.21	50	49.62	−0.76

Fig. 27 DEM AoR from the prediction model validated with the experimental AoR of the free-flowing powder

Table 10 Executed simulation run for the validation of the process model of the AoR and the ε of the cohesive powder

Run	$\mu_{r,pp}$	$\mu_{s,pp}$	e_{pp}	Y (log GPa)	d_S (μm)	C_{pp} (J/m³)	Predicted AoR (°)	DEM AoR (°)	Deviation error of AoR (%)	Predicted ε (%)	DEM ε (%)	Deviation error of ε (%)
54	0.244	0.64	0.051	7.41	694.2	50,000	40	40.8	+2	56.23	54.84	−2.47
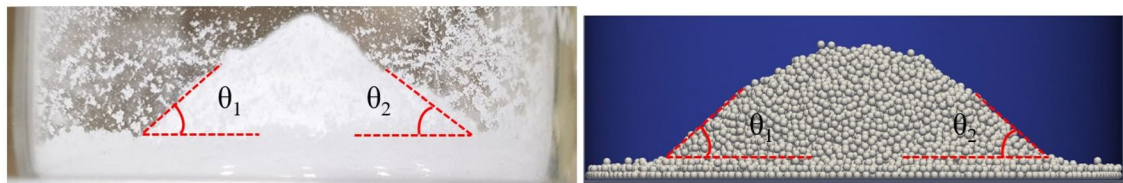
Fig. 28 DEM AoR from the prediction model validated with the experimental AoR of the cohesive powder

can be seen in this study that this depends on the application and not only on the type of powder being used.

The prediction model of the cohesive powder was validated by running a new simulation having $\mu_{s,pp}$ equal to the experimental value. Based on selecting the optimized parameter combination, Table 10 lists the results of the prediction run simulation of the AoR and ε compared and validated with the experimental data.

The very low deviation errors confirm the validity of our study approach, and thus InhaLac 251 (the cohesive powder) was calibrated as well. Moreover, Fig. 28 shows the AoR of run 54 compared with the experimental AoR of the cohesive powder.

5 Summary and conclusions

In the presented work, a semiautomated calibration approach was introduced in which two different powders, i.e., free-flowing and cohesive, were systematically studied and their parameters numerically calibrated using a DEM—experimental data and following regression analysis. The work

aimed, firstly, to perform a systematic statistical parametric study to understand the impact of six interparticle DEM microscopic input parameters on four macroscopic bulk responses and on the computational time. Secondly, numerical validation of the experimental angle of repose and porosity values using a statistical prediction model was performed. The examined microscopic parameters were Young's modulus, particle size, particle–particle coefficient of restitution, static and rolling friction coefficients and cohesion energy density. Interaction properties between particle and wall and between wall and wall were set constant, whereas particle–particle properties were extensively studied. Some of the highlights can be summarized as follows:

- Applying powder characterization using measurement devices decreased the number of needed parameters to be calibrated, which improves the robustness of parameter tuning.
- DoE proved to be an efficient tool in the calibration approach, whereas the regression analysis served in better understanding the impact of different DEM input parameters on the observed responses.

- The quadratic D-optimal design model ascertained its efficiency and reliability in saving computational time by setting up a small optimized number of simulations to be run.
- For the free-flowing study, it was shown that the static friction coefficient has the most significant impact on almost all the output responses. The particle size and stiffness, however, had the highest impact on the computation costs.
- Regarding the cohesive study, the results were in many cases similar to those of the free-flowing study except that the particle stiffness had a negative impact on the angle of repose, and the cohesion energy density had some impact on all the responses. It has been proven in this study that the involvement of cohesion increases the influence of the particle stiffness on some responses, e.g., the angle of repose.
- Scaling up the particle size using the coarse-graining method proved to have no effect on the angle of repose in both studies.
- The built statistical prediction model yielded a good quantitative agreement between the DEM simulation and the experimental result values.

Based on these results, future work will focus on additional numerical and experimental studies under different conditions to determine the validation scope of the selected parameters. One application would be running auger dosing experiments and studying the mass flow rate. This would allow to validate the DEM model using a real-scale machine, subjected to controlled initial and boundary conditions.

Compliance with ethical standards

References

1. Parker RSR, Taylor P (1966) Adhesion and Adhesives. Pergamon Press, Oxford
2. Kapelle R, Schott D (2015) Calibration and verification experiments for discrete element modeling of cohesive materials. Procedia Eng 102:741–748
3. Cundall PA, Strack ODL (1979) A discrete numerical model for granular assemblies. Géotechnique 29:47–65. https://doi.org/10.1192/bjp.115.526.1065
4. Zhu HP, Zhou ZY, Yang RY, Yu AB (2007) Discrete particle simulation of particulate systems: theoretical developments. Chem Eng Sci 62:3378–3396. https://doi.org/10.1016/j.ces.2006.12.089
5. Tsunazawa Y, Shigeto Y, Tokoro C, Sakai M (2015) Numerical simulation of industrial die filling using the discrete element method. Chem Eng Sci 138:791–809. https://doi.org/10.1016/j.ces.2015.09.014
6. Markauskas D, Kačianauskas R (2006) Compacting of particles for biaxial compression test by the discrete element method. J Civ Eng Manag 12:153–161. https://doi.org/10.1080/13923730.2006.9636387
7. Marigo M, Cairns DL, Davies M et al (2010) Developing mechanistic understanding of granular behaviour in complex moving geometry using the Discrete Element Method Part B: investigation of flow and mixing in the Turbula® mixer. Comput Model Eng Sci 59:217–238. https://doi.org/10.1016/j.powtec.2011.04.009
8. Matuttis HG, Luding S, Herrmann HJ (2000) Discrete element simulations of dense packings and heaps made of spherical and non-spherical particles. Powder Technol 109:278–292
9. Dutt M, Hancock B, Bentham C, Elliott J (2005) An implementation of granular dynamics for simulating frictional elastic particles based on the DL_POLY code. Comput Phys Commun 166:26–44. https://doi.org/10.1016/j.cpc.2004.10.006
10. Liu L, Kafui KD, Thornton C (2010) Impact breakage of spherical, cuboidal and cylindrical agglomerates. Powder Technol 199:189–196. https://doi.org/10.1016/j.powtec.2010.01.007
11. Hou QF, Dong KJ, Yu AB (2014) DEM study of the flow of cohesive particles in a screw feeder. Powder Technol 256:529–539. https://doi.org/10.1016/j.powtec.2014.01.062
12. Kretz D, Callau-Monje S, Hitschler M et al (2016) Discrete element method (DEM) simulation and validation of a screw feeder system. Powder Technol 287:131–138. https://doi.org/10.1016/j.powtec.2015.09.038
13. Owen PJ, Cleary PW (2009) Prediction of screw conveyor performance using the Discrete Element Method (DEM). Powder Technol 193:274–288. https://doi.org/10.1016/j.powtec.2009.03.012
14. Obaid A, Turek S, Heider Y, Markert B (2017) A new monolithic Newton-multigrid-based FEM solution scheme for large strain dynamic poroelasticity problems. Int J Numer Meth Eng 109:1103–1129. https://doi.org/10.1002/nme.5315
15. Pillai U, Heider Y, Markert B (2018) A diffusive dynamic brittle fracture model for heterogeneous solids and porous materials with implementation using a user-element subroutine. Comput Mater Sci 153:36–47. https://doi.org/10.1016/j.commatsci.2018.06.024
16. Heider Y, Reiche S, Siebert P, Markert B (2018) Modeling of hydraulic fracturing using a porous-media phase-field approach with reference to experimental data. Eng Fract Mech 202:116–134. https://doi.org/10.1016/j.engfracmech.2018.09.010
17. Prabhu B (2005) Microstructural and mechanical characterization of Al-Al2O3 nanocomposites synthesized by high-energy milling. University of Central Florida
18. Marigo M, Cairns DL, Bowen J et al (2014) Relationship between single and bulk mechanical properties for zeolite ZSM5 spray-dried particles. Particuology 14:130–138. https://doi.org/10.1016/j.partic.2013.05.006

19. Jones R (2003) From single particle AFM studies of adhesion and friction to bulk flow: forging the links. Granul Matter 4:191–204. https://doi.org/10.1007/s10035-002-0122-6

20. Roessler T, Richter C, Katterfeld A, Will F (2018) Development of a standard calibration procedure for the DEM parameters of cohesionless bulk materials—part I: solving the problem of ambiguous parameter combinations. Powder Technol 343:803–812. https://doi.org/10.1016/j.powtec.2018.11.034

21. Marigo M, Stitt EH (2015) Discrete element method (DEM) for industrial applications: comments on calibration and validation for the modelling of cylindrical pellets. KONA Powder Part J 32:236–252. https://doi.org/10.14356/kona.2015016

22. Al-hashemi HMB, Al-amoudi OSB (2018) A review on the angle of repose of granular materials. Powder Technol 330:397–417. https://doi.org/10.1016/j.powtec.2018.02.003

23. Coetzee CJ (2017) Review: calibration of the discrete element method. Powder Technol 310:104–142. https://doi.org/10.1016/j.powtec.2017.01.015

24. Liu SD, Zhou ZY, Zou RP et al (2014) Flow characteristics and discharge rate of ellipsoidal particles in a flat bottom hopper. Powder Technol 253:70–79. https://doi.org/10.1016/j.powtec.2013.11.001

25. Zhou YC, Xu BH, Yu B, Zulli P (2002) An experimental and numerical study of the angle of repose of coarse spheres. Powder Technol 125:45–54. https://doi.org/10.1109/MACE.2011.5986910

26. Yan Z, Wilkinson SK, Stitt EH, Marigo M (2015) Discrete element modelling (DEM) input parameters: understanding their impact on model predictions using statistical analysis. Comput Part Mech 2:283–299. https://doi.org/10.1007/s40571-015-0056-5

27. Lommen S, Schott D, Lodewijks G (2014) DEM speedup: stiffness effects on behavior of bulk material. Particuology 12:107–112. https://doi.org/10.1016/j.partic.2013.03.006

28. Boukouvala F, Gao Y, Muzzio F, Ierapetritou MG (2013) Reduced-order discrete element method modeling. Chem Eng Sci 95:12–26. https://doi.org/10.1016/j.ces.2013.01.053

29. El Kassem B, Brinz T, Heider Y, Markert B (2018) Experimental study and discrete element simulation of auger dosing of different pharmaceutical powders. Proc Appl Math Mech PAMM. https://doi.org/10.1002/pamm.201800261

30. Souihi N, Josefson M, Tajarobi P et al (2013) Design space estimation of the roller compaction process. Ind Eng Chem Res 52:12408–12419

31. Wilkinson SK, Turnbull SA, Yan Z et al (2017) A parametric evaluation of powder flowability using a Freeman rheometer through statistical and sensitivity analysis: a discrete element method (DEM) study. Comput Chem Eng 97:161–174. https://doi.org/10.1016/j.compchemeng.2016.11.034

32. Johnstone MW (2010) Calibration of DEM models for granular materials using bulk physical tests. PhD thesis. The University of Edinburgh

33. Benvenuti L, Kloss C, Pirker S (2016) Identification of DEM simulation parameters by Artificial Neural Networks and bulk experiments. 291:456–465. https://doi.org/10.1016/j.powtec.2016.01.003

34. Rackl M, Hanley KJ (2017) A methodical calibration procedure for discrete element models. Powder Technol 307:73–83. https://doi.org/10.1016/j.powtec.2016.11.048

35. Wei H, Tang X, Ge Y et al (2019) Numerical and experimental studies of the effect of iron ore particle shape on repose angle and porosity of a heap. Powder Technol 353:526–534. https://doi.org/10.1016/j.powtec.2019.05.031

36. Li T, Li C, Li C et al (2019) ScienceDirect Porosity of flowing rice layer: experiments and numerical simulation. Biosyst Eng 179:1–12. https://doi.org/10.1016/j.biosystemseng.2018.12.003

37. Cheng H, Shuku T, Thoeni K, Yamamoto H (2018) Probabilistic calibration of discrete element simulations using the sequential quasi-Monte Carlo filter. Granul Matter 20:1–19. https://doi.org/10.1007/s10035-017-0781-y

38. Do HQ, Aragón AM, Schott DL (2017) Automated discrete element method calibration using genetic and optimization algorithms. In: EPJ Web of conferences, p 15011

39. Soltanbeigi B, Podlozhnyuk A, Papanicolopulos SA et al (2018) DEM study of mechanical characteristics of multi-spherical and superquadric particles at micro and macro scales. Powder Technol 329:288–303. https://doi.org/10.1016/j.powtec.2018.01.082

40. Labra C, Ooi JY, Sun J (2013) Spatial and temporal coarse-graining for DEM analysis. AIP Conf Proc 1542:1258–1261. https://doi.org/10.1063/1.4812167

41. Brini E, Algaer EA, Ganguly P et al (2013) Systematic coarse-graining methods for soft matter simulations—a review. Soft Matter 9:2108–2119. https://doi.org/10.1039/c2sm27201f

42. Bierwisch C, Kraft T, Riedel H, Moseler M (2009) Three-dimensional discrete element models for the granular statics and dynamics of powders in cavity filling. J Mech Phys Solids 57:10–31. https://doi.org/10.1016/j.jmps.2008.10.006

43. Weinhart T, Labra C, Luding S, Ooi JY (2015) Influence of coarse-graining parameters on the analysis of DEM simulations of silo flow. Powder Technol 293:138–148. https://doi.org/10.1016/j.powtec.2015.11.052

44. Kloss C, Goniva C, Hager A et al (2012) Models, algorithms and validation for opensource DEM and CFD-DEM. Prog Comput Fluid Dyn Int J 12:140. https://doi.org/10.1504/PCFD.2012.047457

45. Wensrich CM, Katterfeld A (2012) Rolling friction as a technique for modelling particle shape in DEM. Powder Technol 217:409–417. https://doi.org/10.1016/j.powtec.2011.10.057

46. Derakhshani SM, Schott DL, Lodewijks G (2015) Micro – macro properties of quartz sand: experimental investigation and DEM simulation. Powder Technol 269:127–138. https://doi.org/10.1016/j.powtec.2014.08.072

47. Zhou D, Qiu Y (2010) Understanding material properties in pharmaceutical product development and manufacturing: powder flow and mechanical properties. J Valid Technol 73:65–77. https://doi.org/10.6061/clinics/2018/e264

48. Beach LE (2011) Effect of dry particle coating on the properties of cohesive pharmaceutical powders. Eur J Pharm Sci 43(4):325–333

49. Krantz M, Zhang H, Zhu J (2009) Characterization of powder flow: static and dynamic testing. Powder Technol 194:239–245. https://doi.org/10.1016/j.powtec.2009.05.001

50. Emery E, Oliver J, Pugsley T et al (2009) Flowability of moist pharmaceutical powders. Powder Technol 189:409–415. https://doi.org/10.1016/j.powtec.2008.06.017

51. Lumay G, Boschini F, Traina K et al (2012) Measuring the flowing properties of powders and grains. Powder Technol 224:19–27. https://doi.org/10.1016/j.powtec.2012.02.015

52. Hertz H (1881) On contact between elastic bodies. J Reine Angew Math 171:156–171

53. Mindlin R (1949) Compliance of elastic bodies in contact. ASME Trans J Appl Mech 16:259–268

54. Vizcarra GC, Nimbalkar S, Casagrande M (2016) Modeling behaviour of railway ballast in prismoidal apparatus using discrete element method. Proc Eng 143:1177–1184. https://doi.org/10.1016/j.proeng.2016.06.125

55. Syed Z, Tekeste M, White D (2017) A coupled sliding and rolling friction model for DEM calibration. J Terramechanics 72:9–20. https://doi.org/10.1016/j.jterra.2017.03.003

56. Ai J, Chen JF, Rotter JM, Ooi JY (2011) Assessment of rolling resistance models in discrete element simulations. Powder Technol 206:269–282. https://doi.org/10.1016/j.powtec.2010.09.030

57. Iwashita K, Oda M (2000) Micro-deformation mechanism of shear banding process based on modified distinct element method. Powder Technol 109:192–205. https://doi.org/10.1016/S0032-5910(99)00236-3

58. Johnson KL, Kendall K, Roberts AD (1971) Surface energy and the contact of elastic solids. Proc R Soc A Math Phys Eng Sci 324:301–313. https://doi.org/10.1098/rspa.1971.0141

59. Li Y, Xu Y, Thornton C (2005) A comparison of discrete element simulations and experiments for "sandpiles" composed of spherical particles. Powder Technol 160:219–228. https://doi.org/10.1016/j.powtec.2005.09.002

60. Boac JM, Casada ME, Maghirang RG, Harner JP (2010) Material and interaction properties of selected grains and oilseeds for modeling discrete particles. Trans ASABE 53:1201–1216. https://doi.org/10.13031/2013.32577

61. Li Z, Yang J, Xu X et al (2002) Particle shape characterization of fluidized catalytic cracking catalyst powders using the mean value and distribution of shape factors. Adv Powder Technol 13:249–263

62. Carr RL (1965) Evaluating flow properties of solids. Chem Eng 72:163–168

63. (2018) About the FT4 powder rheometer: shear testing. In: Free Technol https://www.freemantech.co.uk/powder-testing/ft4-powder-rheometer-powder-flow-tester/shear-testing. Accessed 26 Jan 2020

64. Worku ZA, Kumar D, Gomes JV et al (2017) Modelling and understanding powder flow properties and compactability of selected active pharmaceutical ingredients, excipients and physical mixtures from critical material properties. Int J Pharm 531:191–204. https://doi.org/10.1016/j.ijpharm.2017.08.063

65. Freeman R (2007) Measuring the flow properties of consolidated, conditioned and aerated powders—a comparative study using a powder rheometer and a rotational shear cell. Powder Technol 174:25–33. https://doi.org/10.1016/j.powtec.2006.10.016

66. (2018) Why are powders complex? The three phases of powder. In: Free. Technol. https://www.freemantech.co.uk/_powders/powder-flowability-bulk-properties-of-powders. Accessed 16 Mar 2019

67. Sundararajan K (2018) Design of experiments—a primer. https://www.isixsigma.com/tools-templates/design-of-experiments-doe/design-experiments-☼-primer/. Accessed 2 Apr 2019

68. Geuzaine C, Remacle J-F (2017) A three-dimensional finite element mesh generator with built-in pre- and post-processing facilities. Int J Numer Meth Engng 79:1309–1331. https://doi.org/10.1002/nme.2579

69. MakeItFrom (2019) EN 1.4404 (X2CrNiMo17-12-2) Stainless Steel. https://www.makeitfrom.com/material-properties/EN-1.4404-X2CrNiMo17-12-2-Stainless-Steel. Accessed 19 Jan 2019

70. Roessler T, Katterfeld A (2018) Scaling of the angle of repose test and its influence on the calibration of DEM parameters using upscaled particles. Powder Technol 330:58–66. https://doi.org/10.1016/j.powtec.2018.01.044

71. Coetzee CJ (2016) Calibration of the discrete element method and the effect of particle shape. Powder Technol 297:50–70. https://doi.org/10.1016/j.powtec.2016.04.003

72. Briend R, Radziszewski P, Pasini D (2011) Virtual soil calibration for wheel-soil interaction simulations using the discrete-element method. Can Aeronaut Space J 57:59–64

73. Just S, Toschkoff G, Funke A et al (2013) Experimental analysis of tablet properties for discrete element modeling of an active coating process. AAPS PharmSciTech 14:402–411. https://doi.org/10.1208/s12249-013-9925-5

74. Combarros M, Feise HJ, Zetzener H, Kwade A (2014) Segregation of particulate solids: experiments and DEM simulations. Particuology 12:25–32. https://doi.org/10.1016/j.partic.2013.04.005

75. Boikov AV, Savelev R, Payor VA (2018) DEM calibration approach: design of experiment DEM calibration approach: design of experiment. J Phys Conf Ser. https://doi.org/10.1088/1742-6596/1015/3/032017

Publisher's Note Springer Nature remains neutral with regard to jurisdictional claims in published maps and institutional affiliations.